University of Stavanger

FACULTY OF SCIENCE AND TECHNOLOGY

MASTER'S THESIS

Study programme/specialisation: Marine and Offshore Technology	Spring semester, 2020 Open access
Author: Ivan Ekerhovd	
Programme coordinator: Prof. Muk Chen Ong Supervisor(s): Prof. Muk Chen Ong and Dr. Wenhua Zhao	
Title of master's thesis: Numerical study on gap resonance coupled to vessel motions relevant to side-by-side offloading	
Credits: 30	
Keywords: Gap Resonance, Hydrodynamics, Vessel Motions, Side-by-Side Offloading	Number of pages: 91 + supplemental material/other: 95 Stavanger, 13.07.2020

Abstract

Floating Liquefied Natural Gas (FLNG) systems are large facilities dealing with offshore storage, processing, and transport of natural gas from the ocean basin. These enormous vessels allow the natural gas to be produced closer to the source, creating advantages for gas export as it can be offloaded directly to an LNG carrier at the facility. During the offloading process, where one vessel is moored alongside the other, a long narrow gap is created between them. These side-by-side operations are of limited duration and will not take place in severe sea states. However, at certain frequencies, even calm sea states may excite resonant fluid motions in the gap. For any highly resonant system, the amplitude of the response is dependent on the system damping where the resonance may be excited in a linear or non-linear form. For practical applications, the amplitude of the gap resonance during offshore operations in calm sea has shown to be important by itself or due to coupling with vessel motions. There have been studies on the hydrodynamic performance of the gap resonant phenomenon. It remains unclear how the vessel motions will couple with the gap resonance. To investigate the effect of vessel motions on the gap resonance phenomenon, the a series of numerical simulations based on the linear potential flow solver WADAM are conducted in the present study. The numerical model is validated against experimental data which have been publicly available, where the viscous damping coefficient is calibrated as well. The gap resonances are investigated for various configurations, e.g. fixed + fixed vessels, floating + fixed vessels and floating + floating vessels. The most striking phenomenon is that the first gap resonant peak, which is obtained in the case of two fixed vessels, disappears when one of the two or both vessels are allowed to move freely. It is believed to be a result of the added mass effect from sway and heave motions of the floating vessel.

Acknowledgments

This work has been carried out under the supervision of Prof. Muk Chen Ong from Marine and Offshore Technology at the University of Stavanger, and Dr. Wenhua Zhao from Oceans Graduate School at The University of Western Australia.

Firstly, I would like to express my sincere gratitude to my supervisor Prof. Muk Chen Ong for giving me the opportunity to perform this research in cooperation with the research center at The University of Western Australia. I would also like to thank him for always motivating and pushing me to work consistently through the entire semester. The outcome of the thesis would not be of this high standard without his help.

Secondly, I would like to thank my co-supervisor Dr. Wenhua Zhao, who very professionally hosted my visit at Oceans Graduate School of the University of Western Australia, though I had to move back to Norway earlier than planned due to the COVID-19. However, Dr. Zhao continued to supervise me remotely through to the completion of this thesis. He has always been very kind and helpful, and his knowledge about the investigated phenomenon has been of great value.

I would also like to thank Dr. Zhiyuan Pan for sharing his knowledge and experiences with potential flow codes and DNV-GL software which is the core of this thesis.

Finally, I would like to thank my co-students who have always been there for me in need of help. They know who they are.

Stavanger, Norway *Ivan W. Ekerhovd*

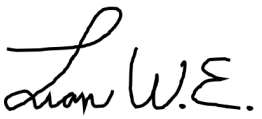

July 13th, 2020

Table of contents

List of figures

List of tables

Chapter 1

Introduction

1.1 Background and Motivation

Floating Liquefied Natural Gas (FLNG) systems are large facilities dealing with offshore storage, processing, and transport of natural gas from the ocean basin (Zhao et al., 2011). These enormous vessels have been developed as a game changer in the offshore industry for unlocking stranded gas reserves from previously uneconomic or unapproachable gas fields. This provides the end users with outcomes of increased efficiency, safer operations, and a reduction in infrastructure maintenance. The systems also allow gas to be produced closer to the source, creating advantages for gas export as it can be offloaded directly to an LNG carrier at the facility.

Transferring liquid cargo from the FLNG facility to an LNG carrier can be done either through a side-by-side configuration or through tandem offloading. In tandem offloading, the vessels are placed around 60 m apart and dynamic positioning is required. The tandem procedure has several disadvantages compared to side-by-side offloading, such as installation of specific transfer machinery in the bow area and the need of long cryogenic pipes. However, for the side-by-side offloading, there are challenges concerning gap resonance as the fluid inside the narrow gap may experience significant resonant response when excited at certain wave frequencies. Transferring cargos through side-by-side configuration is carried out between ships placed alongside each other in calm sea states. Offloading is sensitive to variable weather and ocean conditions, side-to-side rotation of the LNG carrier, wave motions and various filling conditions of liquid cargo.

The background of the present thesis is based on numerical simulations done by Zhao et al. (2018*a*) concerning the gap resonance problem. Their numerical simulations correspond to side-by-side model scaled experiments at the Deepwater Wave Basin at Shanghai Jiao Tong University (Zhao et al., 2017*a*).

Gap resonance is a phenomenon facing numerous challenges as several scenarios are yet to be reported. Previous work shows that linear potential flow theory overpredicts the responses related to the experiment (Pauw et al., 2007; Faltinsen et al., 2007). Many investigators suggested that viscous effects associated with flow separation and free-surface boundary conditions are the main reasons for the discrepancy between experimental data and the linear potential flow calculations (Kristiansen and Faltinsen, 2008; Molin et al., 2009; Kristiansen and Faltinsen, 2012). Feng and Bai (2015) reported that nonlinearity may induce slight shifts in the resonant frequency by carrying out fully nonlinear numerical simulations. In their study, viscosity effect was not considered.

To improve the agreement between the experimental data and linear potential flow calculations, several methods have been proposed. For instance, Huijsmans et al. (2001) introduced a rigid lid; and thereby the vertical motion in the gap was suppressed completely. Newman (2001) allowed different damping rates for each motion by splitting the gap motion into generalized modes, and Chen (2005) introduced a dissipative damping term in the free surface condition. All these methods achieve satisfactory agreement with the experimental data by introducing an additional damping term. Selection of the additional damping coefficient will generally be empirical, and a robust method is required for practical applications to allow for estimates of the gap resonance efficiently using linear potential flow theory. Zhao et al. (2018*a*) introduced artificial damping to three industry standard potential flow solvers, i.e. WAVELOAD-FD, HydroSTAR and WADAM, to account for the viscous damping effect. The calculated response of the free surface elevations in the gap agreed well with the obtained experimental results.

The gap resonance phenomenon has been investigated in steady-state response both in 2D and 3D. Several 2D investigations have shown that the experimentally determined peak resonant response amplitudes are overpredicted by linear potential flow theory (Faltinsen et al., 2007; Lu et al., 2011). The same effect has been reported in 3D for two fixed vessels in side-by-side configuration, although the overprediction was much smaller (Pauw et al., 2007; Molin et al., 2009; Dinoi et al., 2014).

Gap resonance, and moonpool resonance share similar problems. Molin (2001) investigated modal shapes of the resonant modes based on linear potential flow theory and derived an analytical formula to estimate the natural frequencies. Modes with profiles were reported along and across the moonpool. Natural frequencies of the gap resonant modes were predicted by extending the

approach and modifying the boundary conditions at both ends (Molin, 2001; Molin et al., 2002). Previous attempts to use predictions of moonpool resonant frequencies have been made for the understanding of the gap resonance problem. However, boundary conditions at the gap ends differ from the moonpool problem. Because the ends of the gap are open, and the wave energy can escape. Thus, pure resonant standing waves cannot exist. A complex analysis related to this problem have been carried out by Saitoh et al. (2000), where the flow field near the gap ends have been represented using an asymptotic matching technique.

Most research efforts into the gap resonant response are based on analysis of the maximum resonant amplitude at steady state in regular waves. However, a realistic sea condition is never regular. Due to long time for the gap resonance to build up its maximum amplitude, it is challenging to reach steady state in a tank experiment. Reflected waves from the tank walls may also affect the experiment as time goes by. Watai et al. (2015) reported that the time required for the gap resonance to build up to steady state is also a challenge for time domain simulations. To face the difficulties of achieving a steady state response, behavior of the fluid through transient wave groups has been of interest. Eatock Taylor et al. (2008) simulated the gap resonant response numerically using focused wave groups, based on linear potential flow theory.

The accuracy of the potential flow calculations seems to be dependent on the bilge shapes. For the round bilge case, where flow separation is less important, small overpredictions have been reported. For the square bilge case, where flow separation is inevitable, the resonant response amplitude is largely overestimated. Zhao et al. (2017*a*) performed 3D experiments using transient wave groups, for round and square bilge cases. Substantial and radiation damping was shown to be present, and for round bilge shapes it seemed that the damping was completely caused by laminar boundary layers. Wang et al. (2019) observed that mostly all the viscous dissipation was confined to a slender layer surrounding the floating structures, meaning that the contribution from the flow separation can be negligible and the wall friction is the main contribution to the damping.

1.2 Objectives and Outline of the Thesis

The objectives of the present thesis are as follows:

(i) Build up a validated numerical model for gap response analysis in the frequency domain for two identical fixed barges.

(ii) Use the validated numerical model to investigate gap resonance coupled to vessel motions relevant to side-by-side offloading.

The present numerical model shall be built based on the one made by Zhao et al. (2018*a*). This includes validation of the barge hull and free surface as well as the potential flow codes. To build the model, a series of Sesam software from DNV-GL are used. The barge hull is made using GeniE and imported to HydroD for hydrodynamic analysis. Modification of the potential flow codes are done within HydroD and simulated using the potential flow solver WADAM. Simulations are performed in the frequency domain, where several frequency sets and wave directions are defined to obtain the results.

Furthermore, for simplicity purposes the two barges used to enclose the gap are given the same geometrical shape. In reality a significantly large FLNG vessel would be moored alongside a small LNG tanker, forming a narrow gap between them. The present thesis aims to investigate the gap resonance phenomenon further by focusing on the non-dimensional effects.

Once the present numerical model is validated, it is used to investigate the coupling between vessel motion and gap resonance. This implies numerical calculations of a single floating barge and releasing the motion of one barge in side-by-side configuration while the other is fixed. Further, the validated model is used to investigate the importance of artificial damping in the gap. This is done by extending the gap width all the way up to two times the barge breadth.

The outline of the thesis is as follows:

Chapter 1 states the introduction of the present thesis which consists of the background and motivation, the objectives, and the thesis outline.

Chapter 2 gives the theoretical background concerning the linear potential flow solver used to produce the numerical results in the present thesis. This chapter also explains the gap resonance problem with focus on surface modes and viscous damping.

Chapter 3 describes the methodology behind the present numerical model. This chapter gives information about how the gap resonance between the two barges are analyzed and presents the equations used in the linear potential flow code.

Chapter 4 gives the results of a validation study of two fixed barges in a side-by-side configuration for three different gap widths. The present numerical results are compared against both previous numerical results and experimental data.

Chapter 5 presents the coupling between vessel motions and gap resonance. In this chapter, motions of the barges are released to compare the effects against the fixed case, and to investigate the coupling between vessel motions and gap resonance. Numerical results are presented both in beam sea and head sea conditions where the motion of the free surface is of high interest. This chapter also gives numerical results concerning the influence of gap width and artificial damping of the free surface.

Chapter 6 states the overall conclusions of the present thesis, as well as the recommendations for further work.

Chapter 2

Theoretical Background and Gap Resonance

The numerical calculations in the present thesis are generally performed using linear potential flow codes. In this chapter, the most essential theory behind DNV-GL's potential flow solver WADAM will be presented. This will be valuable to understand the implementation of the present numerical model and obtained numerical results. Furthermore, as this thesis concerns gap resonance, fundamental theory and problems will also be described in this chapter.

2.1 Linear potential flow theory

A linear analysis is usually accurate for predicting global wave frequency loads. Linear theory can, to a large extent, describe wave-induced motions and loads on floating bodies and large-volume structures. However, the non-linear effects may be important in severe sea states, and to describe horizontal motions of moored structures.

Consider a structure with amplitude ξ_0 in incident regular waves where the waves are far from breaking as the wave steepness is small. Linear theory means that the wave-induced motion and load amplitudes are linearly proportional to ξ_0 (Faltinsen, 1990). Results of linear theory is obtained in irregular waves by adding together regular waves with different amplitude, wavelength, and direction. Now, consider a long-crested sea state described by the spectrum $S(\omega)$, surface elevations may be expressed as,

$$\zeta = \sum_{j=1}^{N} \xi_j \sin(\omega_j t - k_j x + \epsilon_j) \tag{2.1}$$

where ξ_j, ω_j, k_j and ϵ_j represents respectively the wave amplitude, angular frequency, wave number and random phase angle of the wave component number j. Due to linearity, the response

of each wave component in Equation (2.1) may be analyzed separately. The steady state response may be written as,

$$\xi_j \left|H(\omega_j)\right| \cdot \sin\left(\omega_j t - \psi(\omega_j) + \epsilon_j\right) \tag{2.2}$$

where $\left|H(\omega_j)\right|$ is the response amplitude per unit wave amplitude, also known as the linear transfer function. The phase angle associated with the response is represented by $\psi(\omega_j)$.

To find the potential function $\varphi(x, y, z, t)$ using potential flow theory requires the assumption of irregular flow $\nabla \times \vec{U} = 0$, and that the flow is incompressible $\nabla \cdot \vec{U} = 0$. These terms are in many cases roughly approximated, where vortex shredding, viscous terms and compressibility have large effect.

Considering the assumption of irregular, incompressible fluid flow, requires that the velocity potential must satisfy the Laplace equation where $\nabla^2 \varphi = 0$:

$$\nabla \cdot \vec{U} = \frac{\partial^2 \varphi}{\partial x}\vec{\imath} + \frac{\partial^2 \varphi}{\partial y}\vec{\jmath} + \frac{\partial^2 \varphi}{\partial z}\vec{k} = 0 \tag{2.3}$$

Based on the mentioned conditions, the equation of potential flow is given by the following equation:

$$\frac{\partial^2 \varphi}{\partial x^2} + \frac{\partial^2 \varphi}{\partial y^2} + \frac{\partial^2 \varphi}{\partial z^2} = 0 \tag{2.4}$$

If the velocity profile is linear, we can obtain the potential function by deriving the velocity potential, hence:

$$\varphi(x, y, t) = \frac{\xi_0 g}{\omega} \frac{coshk(z + d)}{\cosh(kd)} \cos\left(wt - kx\right) \tag{2.5}$$

Table 2.1. Parameter list related to Equation (2.5).

$\boldsymbol{\omega = 2\pi/T}$	Wave angular frequency
$\boldsymbol{\xi_0 = Hs/2}$	Wave amplitude
$\boldsymbol{k = 2\pi/L}$	Wave number
t	Time
$\boldsymbol{g}$	Gravitational acceleration

By using linear wave theory, it is possible to understand the behavior of waves and to give a description of the propagation of waves at the surface layer.

2.1.1 Boundary conditions

To obtain a velocity potential that describes the fluid correctly, boundary conditions must be implemented. Three boundary conditions are used to solve the Laplace equation: free surface boundary condition, wall boundary condition and the bottom boundary condition.

Free surface boundary builds on the fact that the surface will adjust itself to make sure that no water can flow through it. There are two different methods of obtaining this.

→ *The kinematic free surface boundary condition* – Fluid particles at the free surface, will remain on the free surface. The surface elevation can be described as $z = \xi(x, y, t)$, and by removing higher order terms and use the free surface as an approximation of z = 0, we obtain the following equation:

$$\frac{\partial \xi}{\partial t} = \frac{\partial \varphi}{\partial z} \quad , \qquad z = 0 \tag{2.6}$$

→ *The dynamic free surface boundary condition* – Pressure at the free surface is constant and must be equal to the atmospheric pressure. By using the linear assumption for small wave amplitudes:

$$g\xi + \frac{\partial \varphi}{\partial t} = 0 \ , \qquad z = 0 \tag{2.7}$$

By combining the two free surface boundary conditions, it is possible to calculate φ by solving the Laplace equation. The equation is given as:

$$\frac{\partial^2 \varphi}{\partial t^2} + g\frac{\partial \varphi}{\partial z} \ , \qquad z = 0 \tag{2.8}$$

All the boundary conditions are linearized, meaning that the waves from the potential function is expressed as sinusoidal waves.

The wall boundary condition states that no fluid can flow through a wall. The present model for validation includes two fixed barges, meaning they will keep the same position through all the simulations. The only changing parameter is the gap width. However, this will not influence the effect of this boundary condition. As the wave direction is set perpendicular to the longitudinal side of the first barge, the wall boundary condition is given as:

$$u|_{x=a} = 0 \ \Rightarrow \qquad \left.\frac{\partial \varphi}{\partial x}\right|_{x=a} = 0 \tag{2.9}$$

The bottom boundary condition includes that there can be no fluid motion through the seabed, assumed at a depth h. Water depth and other environmental conditions are discussed in Section 3.1.1. The horizontal sea bottom condition can be expressed as:

$$w|_{z=-d} = 0 \ \Rightarrow \qquad \left.\frac{\partial \varphi}{\partial z}\right|_{z=-d} = 0 \tag{2.10}$$

2.1.2 Radiation and diffraction potential

Regular waves are waves with one amplitude and one frequency. By using first order, linear wave potential including linearized Bernoulli and boundary conditions, the problem may be divided into two separate problems called radiation and diffraction potentials.

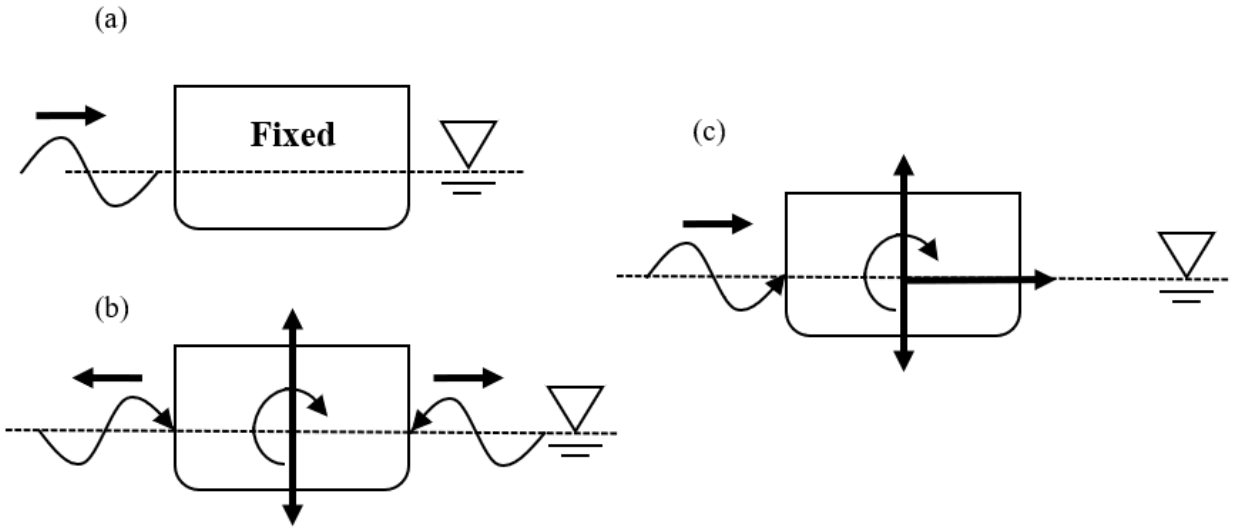

Figure 2.1. Superposition of the radiation and diffraction problem.

The radiation and diffraction potential are solved separately in WADAM. The radiation problem is solved due to the oscillations of the floating bodies, and the incident waves are diffracted from the bodies. In the diffraction problem shown in Figure 2.1 (a), the body is assumed to be in incident regular waves and constrained from oscillating. In the radiation problem shown in Figure 2.1 (b), there are no incident waves, meaning that the body is forced to oscillate with the wave excitation frequency. By solving these problems separately, a floating body oscillating in incident waves is then considered, see Figure 2.1 (c).

Total unsteady potential φ for a sinusoidal wave excitation with angular frequency ω, is produced by the sum of the incident wave velocity potential φ_I, the diffracted wave velocity potential φ_D and the radiated wave velocity potential φ_R. By adding the radiated and diffracted wave velocity potentials together, the scattered velocity potential φ_S may be obtained. Total unsteady linear potential for a sinusoidal wave excitation may be expressed as,

$$\varphi(x,y,z,t) = \left[\varphi_{\mathrm{I}}(x,y,z) + \varphi_D(x,y,z) + \sum_{R=1,2,6} \xi_R \varphi_R\right] e^{-i\omega t} \tag{2.11}$$

The incident wave potential $\varphi_{\mathrm{I}}(x,y,z)$ represents the incident waves, the diffraction potential $\varphi_D(x,y,z)$ represents the disturbance of the incident waves diffracted from the body, while the radiation potential $\varphi_R(R = 1,2,6)$ is due to surge, heave and pitch (only motions on the vertical plane). The incident wave potential in deep water is,

$$\varphi_{\mathrm{I}} = -\frac{\xi_0 g i}{\omega} e^{kz} e^{i(kx\,cos\alpha + ky\,sin\alpha)} \tag{2.12}$$

where α represents the wave heading. In this thesis, 90 and 270 degrees are used for the beam sea, while 0 degrees represents the head sea. The total unsteady potential should be satisfied in the fluid domain, on the free surface, on the submerged body surface, on the seabed, as well as for far field radiation condition at infinity. The integral equation satisfied by the radiation velocity potentials φ_R on the boundary, is expressed as,

$$2\pi\varphi_R(x) + \iint_{Sb} \varphi_R(\xi) \frac{\partial G(\xi;x)}{\partial n_\xi} d\xi = \iint_{Sb} n_R G(\xi;x) d\xi \tag{2.13}$$

where Sb represents body mean wet surface. The Green function $G(\xi;x)$ represents the velocity potential at the field point x due to a point source located at point ξ. The integral equation for the diffraction velocity potential is,

$$2\pi\varphi_D(x) + \iint_{Sb} \varphi_D(\xi) \frac{\partial G(\xi;x)}{\partial n_\xi} d\xi = 4\pi\varphi_I(x) \tag{2.14}$$

2.2 Equation of motion in the frequency domain

By solving the dynamic equilibrium equation for regular waves at different frequencies, the dynamic motion characteristics of a floating body may be obtained. In WADAM, the equation of motion is established for harmonic motion of rigid body systems expressed in the global coordinate system (DNV-GL, 2017). The motion vector $X(\omega, \alpha)$ can be found from the equation of motion by applying newtons law and including added mass, damping, and exciting force contribution acting on the panel,

$$[-\omega^2\big(M + A(\omega)\big)\, i\omega(B(\omega)_P + B_v) + C + C_e]\, X(\omega, \alpha) = F(\omega, \alpha) \tag{2.15}$$

The equation of motion is solved to obtain the linear transfer functions (RAOs) of the desired vessel motions. Table 2.2 shows the parameters related to Equation (2.15).

Table 2.2. Parameters used in the equations of motion.

$\boldsymbol{M}$	6 by 6 body inertia matrix
$\boldsymbol{A(\omega)}$	6 by 6 frequency dependent added mass matrix
$\boldsymbol{B(\omega)_P}$	6 by 6 frequency dependent potential damping matrix
$\boldsymbol{B_v}$	6 by 6 linearized viscous damping matrix
$\boldsymbol{C}$	6 by 6 hydrostatic restoring matrix
$\boldsymbol{C_e}$	6 by 6 external restoring matrix
$\boldsymbol{F(\omega, \alpha)}$	6 by 1 complex exciting force vector for ω and heading angle α

2.2.1 Added Mass and Damping

Added mass is the additional mass of a body when accelerated relative to a surrounding fluid. The added mass is generally determined by numerical calculations and experience data where the hull form is evaluated. In this thesis, a frequency dependent added mass matrix is calculated through WADAM's linear potential flow codes.

Damping may be defined as the dissipation of energy for each vibration where the response will decay exponentially for each free damped oscillation. The damping coefficient is connected to critical damping which provides the fastest approach to zero amplitude for a damped oscillator. The damping ratio may be defined as the ratio of critical damping, but in WADAM most of the damping is found from radiation velocity potential.

2.3 Free surface calculation

The linear potential theory as described in Section 2.1 is applied in WADAM to calculate the first-order radiation and diffraction effects on large volume structures. The implementation is based on WAMIT developed by Massachusetts Institute of Technology, where a three-dimensional panel method is used to evaluate the velocity potentials and hydrodynamic coefficients (WAMIT, 2013). The flow is assumed to be ideal and time-harmonic. The non-linear free surface condition is imposed for the second order potential theory computation, while the free surface condition is linearized for the first order. Green's theorem with the free surface source potentials is used as Green's functions to obtain the solution of an integral equation used to determine the radiation and diffraction potentials on the wet part of the body surface. Using the source distribution method, it is possible to evaluate the source strengths using the same source potentials. All source strengths are assumed to be constant over each panel. By using WADAM, the integral equation is solved directly for each frequency.

Furthermore, in the free surface damping methods, a non-zero free surface integral is placed in the gap. This requires paneling of the free surface (gap), and additional gap surface integrals has to be introduced.

2.3.1 Irregular frequencies

A unique solution cannot be obtained at some discrete frequencies and results in sharp jumps in the numerical calculations around these specific frequencies. The phenomenon does not originate from the physical model itself but is a feature of the integral equation. Theoretical analysis for bodies with simple geometries may be used to determine the locations of the discrete irregular frequencies. For the potential inside the body, they are determined from the eigenvalues of the boundary value problem, subject to the linear free surface condition. On the body surface, they are determined by a Dirichlet condition of zero potential. However, for complex structures, it is difficult to determine whether the results have been polluted by irregular frequencies. Multibody analyses are particularly the most difficult cases because similar jumps at resonant frequencies may be present where physical interactions will arise.

Using WADAM, it is possible to remove irregular frequencies with the radiation-diffraction solution. This is done by adding a panel model in the interior water plane. In this thesis, an interior panel model is made on top of the barge hull as a free surface lid. The Green function shown in Equation (2.16), represents velocity potential at the point x, due to the point source ξ (DNV-GL, 2017).

$$\binom{2\pi}{-4\pi}\varphi(x) + \iint_{Sb+Si} \varphi(\xi)\frac{\partial G(\xi;x)}{\partial n_\xi}d\xi = \iint_{Sb}\frac{\partial \varphi(\xi)}{\partial n_\xi}\partial G(\xi;x)d\xi, \qquad x \in \binom{S_b}{S_i} \tag{2.16}$$

where S_b denotes the body mean wet surface, S_i interior free surface, n is the total number of wave frequencies, and φ is the velocity potential.

2.3.2 Damping free surface lids

As earlier mentioned, it is known that free surface elevations in a confined water plane area is overpredicted by linear potential flow theory. Having in mind that the gap between two barge hulls most likely will be affected, WADAM provides an option to suppress the unrealistic free surface elevations. This is done by placing a new panel model on the confined water-plane area, using the following damping free surface conditions (DNV-GL, 2017),

$$\varphi_n = K\varphi(1 - 2i\epsilon - \epsilon^2), \quad at \;\; S_e \tag{2.17}$$

where $K = \omega^2/g$, and ϵ is the linear damping factor on the exterior free surface area S_e. The linear damping factor ϵ can be obtained from model tests and is determined by the geometry of the gap.

In this study, damping factors obtained by Zhao et al. (2018*a*) is used. The integral equation including a panel model of the gap where linear damping is applied can be shown as,

$$\binom{2\pi}{4\pi}\,\varphi(x) + \iint_{Sb} \varphi(\xi)\frac{\partial G(\xi;x)}{\partial n_\xi}d\xi + K(2i\epsilon + \epsilon^2)\iint_{Sb}\frac{\partial G(\xi;x)}{\partial n_\xi}d\xi \tag{2.18}$$

$$= \iint_{Sb}\frac{\partial \varphi(\xi)}{\partial n_\xi}\partial G(\xi;x)d\xi, \qquad x \in \binom{S_b}{S_e}$$

2.4 Gap resonant behavior

A partly closed area of the free surface may be subjected to violent motions at certain frequencies of oscillation. In this thesis, the free surface refers to the gap surface, partly enclosed between two barges. Motion of the gap surface can be triggered in different scenarios:

(i) For fixed bodies
(ii) For bodies free to oscillate
(iii) For bodies forced to oscillate

For fixed and floating structures, motions can be triggered by incident waves. Similarly, gap surface motions may also occur if the structure is forced to oscillate. When the oscillations are caused by forced body motion or incident waves, an infinite number of gap resonant frequencies will be present. At these frequencies, the gap surface will experience large motions, and the surface mode will vary for each resonant frequency. The location of these frequencies depends on the geometrical shape of the investigated body.

2.4.1 Gap surface modes

Each gap resonant frequency is related to its own surface mode. An illustration of two side-by-side barges with mode description is shown in Figure 2.2. These modes are often designated as (m, n), where m describe the transversal direction along the gap, and n the longitudinal direction across the gap. In moonpool situations, the piston-mode is often discussed (Molin, 2001). This would be the case of $n = 0$ and $m = 0$, where the entire surface is moving up and down with no wave energy loss through open boundaries. However, for the gap resonance problem, it is not possible to obtain $m = 0$. Seen in Figure 2.2, dashed lines at each gap end, represents the boundaries connecting the gap with the outside surface. Fluid inside the gap is continuous with fluid outside the boundaries. As the gap surface is moving up and down, the outside fluid is calm.

Thus, no flat surface is present in the gap and the only way to obtain a piston-like behavior would be if the boundaries towards the outside calm water are covered with walls.

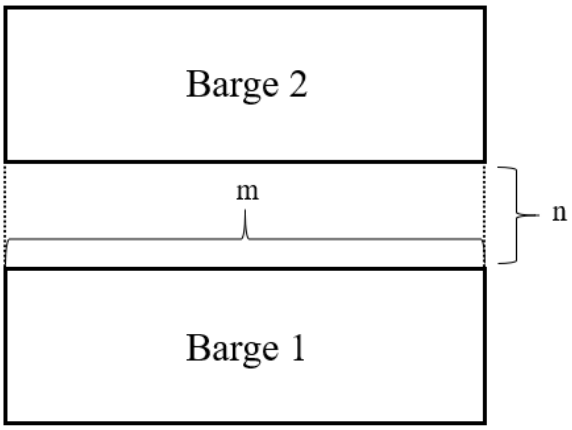

Figure 2.2. Illustration of two barges seen from above showing the designated parameters (m, n) used to describe the different modes of the gap resonance.

Nevertheless, for narrow gaps it is possible to obtain $n = 0$. In this case, the surface elevation from one barge to the other is considered flat. Similarly, if $n = 1$ one half wavelength is present in the gap from Barge 1 towards Barge 2. Illustrations of some m mode shapes can be seen in Figure 2.3, where one half wavelength can also be seen for $m = 1$. Investigations are often based on the odd modes as they correspond to each resonant peak of the transfer functions. As the horizontal dashed lines in Figure 2.3 represents the boundaries between the surface mode and surrounding fluid, it is important to denote that the boundaries would not be zero for a realistic case but in fact higher.

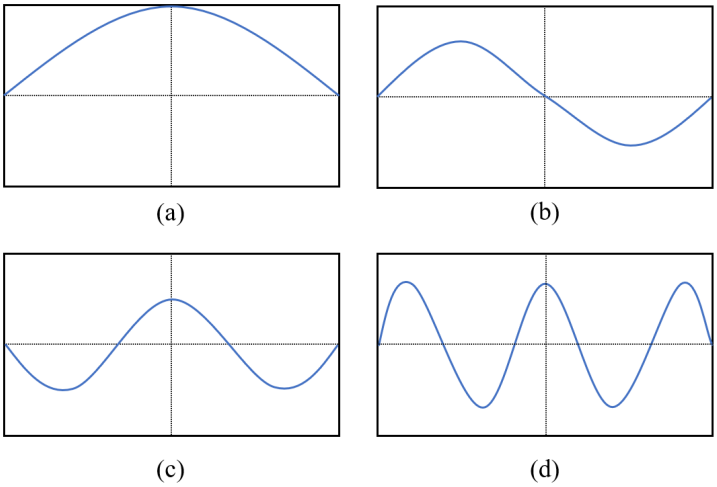

Figure 2.3. Illustration of mode shapes of the resonant response in the gap for (a) $m = 1$, (b) $m = 2$, (c) $m = 3$ and (d) $m = 5$.

2.5 Contribution of Viscous Damping

Codes based on potential theory are effective in many hydrodynamic applications as viscous contributions are considered small. However, as earlier discussed, experimental data shows that linear potential calculations overpredicts the fluid velocities (Pauw et al., 2007; Faltinsen et al., 2007). Viscous damping is of non-linear character, and as the surface motions in the gap may be of great magnitude, it is reasonable to expect viscous damping to be a considerable contribution to the total damping. Accurate numerical calculations of the viscous effects can be demanding, thereby empirical formulas to approximate the viscous effects are of great value. A general expression for the viscous force acting on an oscillating body in an unbounded fluid may be shown as,

$$F_D = \frac{1}{2}\rho L^2 C_D |v| v \tag{2.19}$$

where ρ is the fluid density, L is the characteristic length, C_D is the drag coefficient, and v is the relative velocity between the body and fluid. Two different contributions to the viscous force

acting on the fluid in the gap will be considered. The first being the effect of skin friction, and the second being the vortex shedding at the bilge corners. Vortex shedding may also be referred to as eddy-making damping. The total viscous force may be expressed as,

$$F_v = F_e + F_f \tag{2.20}$$

where F_e is the viscous contribution due to vortex shedding, and F_f is the viscous contribution due to skin friction.

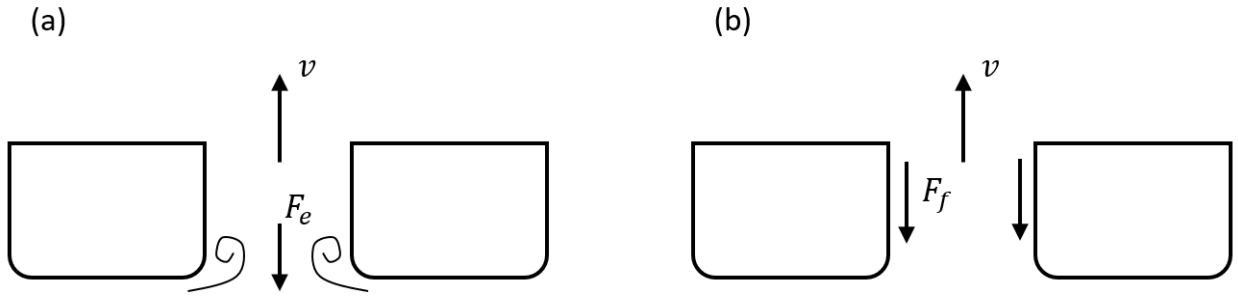

Figure 2.4. Illustration of vortex shedding at bilge corners (a), and illustration of friction force in the gap (b).

The internal forces acting between particles as a fluid flows over a body surface causes the skin friction stress. This viscous effect mainly occurs in immediate vicinity with the body surface. As seen in Figure 2.4 (a), the effect of the stress is a tangential friction force acting in the opposite direction of the relative velocity between the fluid and the barge surface. Friction force is only considered on the wetted surface of the barges on each side of the gap. As the velocities elsewhere will be relatively small, the friction force is considered negligible.

Referring to Figure 2.4 (b), eddy damping is the effect associated with vortex shedding at the bilge corners. In this thesis, a series of gap widths will be analyzed. As the gap width increases, the effect of the vortices will have lower influence on the results.

In this thesis, the contributions of viscous damping are accounted for by applying artificial damping to the free surface of the gap. The artificial damping has been tuned according to the experiments done by Zhao et al. (2017*a*).

Chapter 3

Methodology and Numerical Model

3.1 Hydrodynamic analysis in the frequency domain

Frequency domain analyses are performed while investigating the hydrodynamic properties on the confined water-plane area between two barges. In order to describe the motion of the gap, several frequency sets and wave directions must be determined. By running a WADAM analysis using panel models, it is possible to calculate the hydrodynamic loads and responses from potential theory, as described in Section 2.1. The accuracy of the analysis results may be improved by changing the frequency set and panel mesh.

3.1.1 Environmental conditions

As the investigated barge has a rectangular geometrical shape, different wave directions will result in different Response Amplitude Operators (RAOs). Zhao et al. (2017*a*) performed experiments in the Deepwater Wave Basin at Shanghai Jiao Tong University in both head and beam sea states. In this thesis, the present model will be validated against the numerical model made by Zhao et al. (2018*a*) in beam sea before it can be used to investigate further phenomena. Once it is validated, several other wave directions will also be applied. The location is described by inputs for water depth, density, kinematic viscosity, air density and gravitational acceleration in all frequency domain analyses. Table 3.1 shows the environmental location values. An illustration of the present validation case is shown in Figure 3.1. The water depth is set to 10 m as done in the lab scaled experiment at the Deepwater Wave Basin.

Table 3.1. Environmental condition inputs in WADAM

Gravity [m/s^2]	9.80665
Air Density [kg/m^3]	1.226
Air Kinematic viscosity [m^2/s]	1.462E-005
Water Density [kg/m^3]	1000
Water Kinematic viscosity [m^2/s]	1.19E-006
Water Depth [m]	10

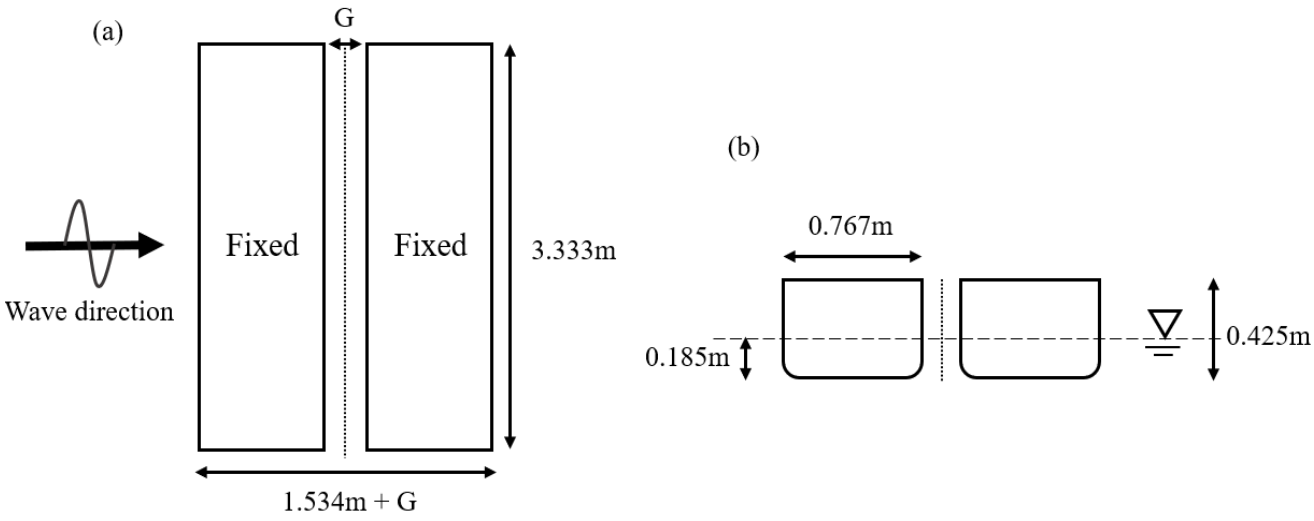

Figure 3.1. Illustration of the two identical side-by-side fixed barge hulls

Figure 3.1 (a) illustrates the barge hulls from above subjected to beam sea. The gap width is defined as *G*, where three different values are used to validate the present model. A more detailed description about the gap widths will be shown in Section 4, where damping values are displayed in Table 4.1. Figure 3.1 (b) illustrates the draft of the barge hulls seen from the front. In the numerical simulations, the structure below the draft is the only part needed to perform the analysis. Following the case done by Zhao et al. (2018*a*), the models are created with round corners at both bilges, and each with a radius of 0.083 m at the entire length of the barge hulls.

3.1.2 Frequency set

A frequency set must be defined to perform the hydrodynamic analysis using a potential flow solver. WADAM can only handle 200 frequencies at a time. If 200 frequencies are not enough for the analysis, smaller frequency sets may be defined to run several cases simultaneously. In the validation case frequencies are defined as $\omega = 4 \sim 10$ rad/s, with an interval of $\Delta\omega = 0.031$ rad/s. This results in a frequency set based on 191 frequencies, to maximize the accuracy of the result. The frequency domain is based on linear solutions of the equations of motions. The equation system can be solved for the response at different frequencies to obtain the linear transfer functions (RAOs) of the surface elevation in the gap. To obtain time histories of the center of the gap, irregular wave realizations may be made. Irregular waves are known to be described as the sum of regular waves, and has all a unique frequency, amplitude, and phase.

3.1.3 Panel model

WADAM is based on a three-dimensional panel method. The panel model used in WADAM may be a single super element or a hierarchy of super elements. It may describe either the entire wet surface or it may take advantage of either one or two planes of symmetry of the wet surface (DNV-GL, 2017). The panel method uses source points, which can be described as elementary solutions of the Laplace equation. The Laplace equation is solved for the inviscid, incompressible flow, where the panel model has been described as an ideal flow element. The barge is described by the panel elements forming the hull and flow properties are calculated for each of the panel elements. The method is based on potential theory, meaning oscillations are assumed to be small compared to the cross-sectional dimensions of the body itself. Figure 3.2 shows the panel model designed to describe the surface of the barge during the forthcoming investigations.

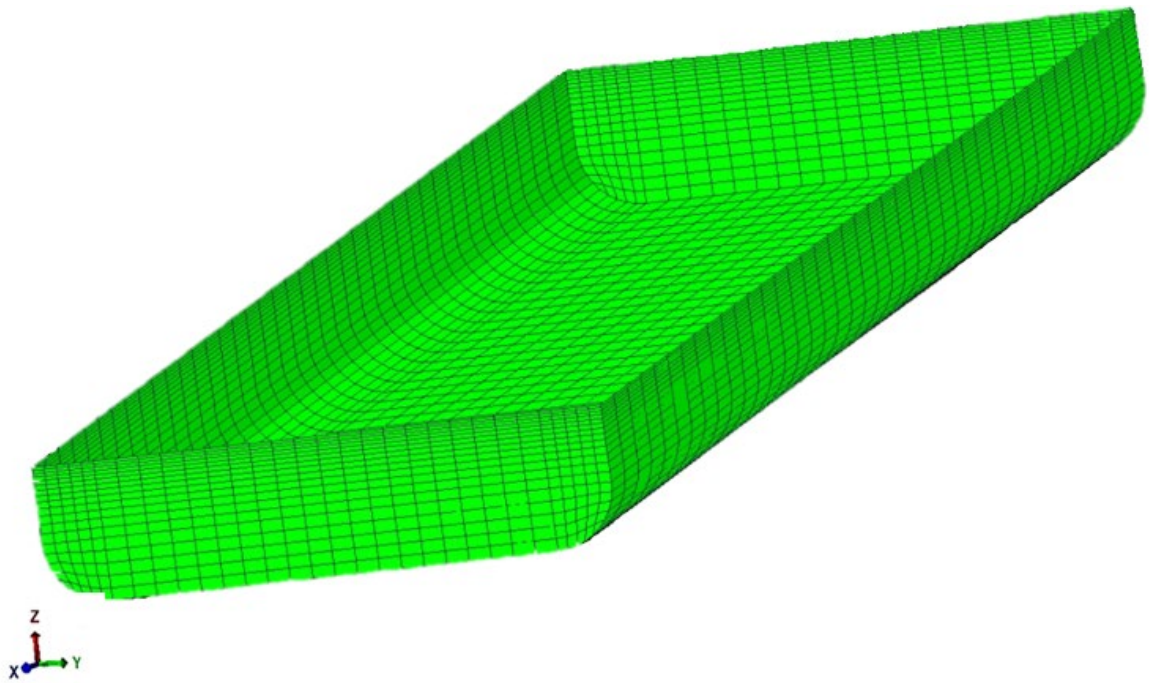

Figure 3.2. Panel model of the barge hull created in GeniE with a mesh of 3720 elements.

The barge geometry in the present study is modelled through a panel model, representing the shape of the barge hull. The panel model defining the hull geometry is created in GeniE and exported to HydroD for hydrodynamic analysis. As earlier mentioned, the two barges are based on the geometry of a Floating liquefied natural gas (FLNG) facility and an LNG carrier, but in this case at lab scale. To analyze the response in the gap, three panel models are created. The first one being the barge hull itself, created in GeniE. However, the others are created in HydroD as free-surface-lids.

As explained in Section 2.3.1, in order to remove the irregular frequencies, a lid on the internal water plane of the barge is developed. This is done by creating a mesh on the free surface on top of the barge hull. A free surface mesh may be created at the specified loading condition by utilizing another feature in HydroD called Hydromesh. To provide external damping in the gap, a so-called damping lid is placed at the free surface of the gap. The damping term is proportional to a damping coefficient, where the damping effect must be tuned to match the experimental results. This has already been done by Zhao et al. (2018*a*) and in this thesis the same damping coefficients will be implemented to validate the present model.

By refering to Figure 3.3, the barge hull mesh is displayed in green. Further, the interior free surface is covered with an internal lid for irregular frequency removal, shown in blue. The gap is covered with a damping lid displayed in pink. For the WADAM analysis, symmetri is used to obtain two barge hulls with internal lids on both sides of the gap lid.

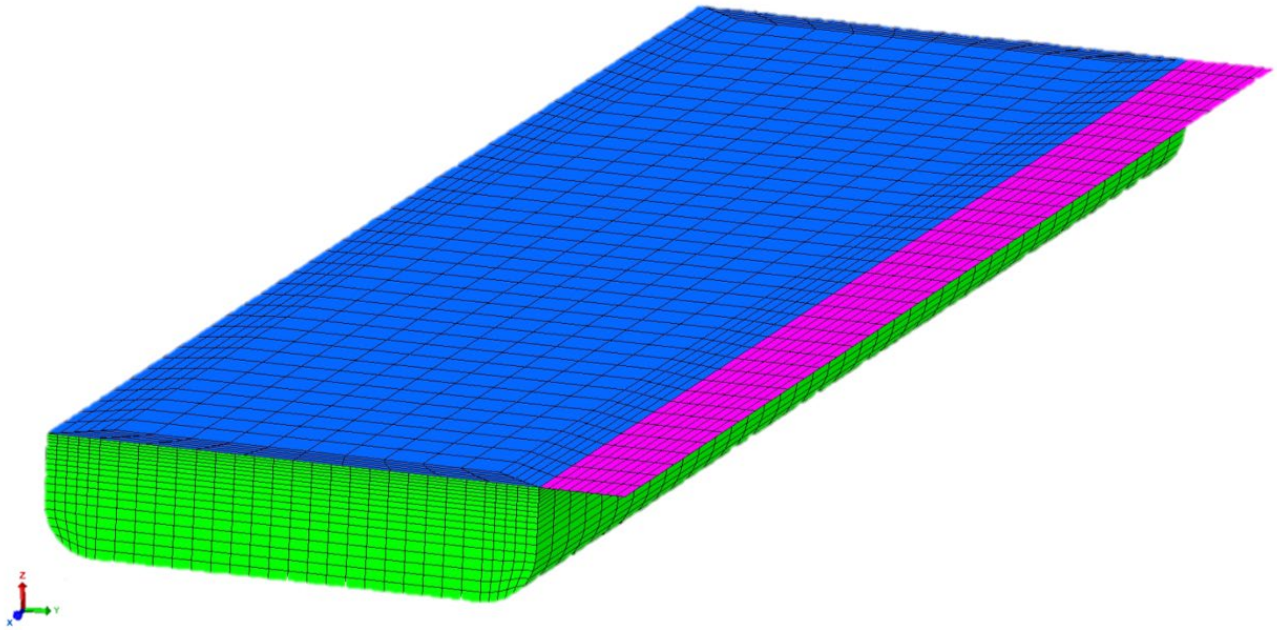

Figure 3.3. Panel models used to create the present case, here with G = 66 mm.

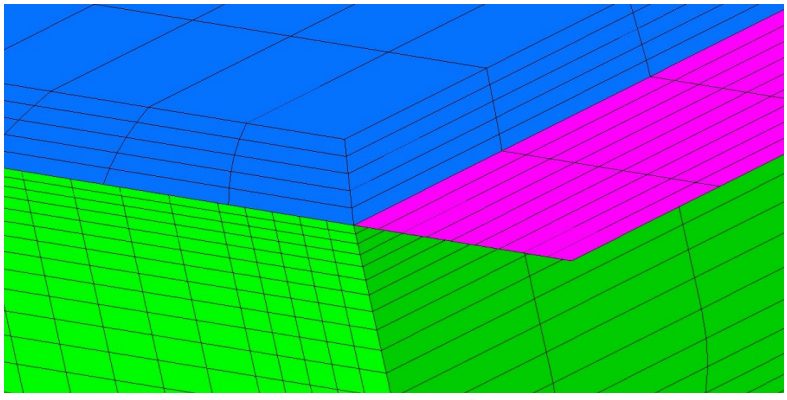

Figure 3.4. Close up showing the refinements of the mesh towards the waterline area.

The panel grid on the hull surface has a great impact on the accuracy of the calculations and have a large effect on the predicted response. The panel density should be large in areas with rapid changes in flow, such as corners and edges towards the waterline area. In order to validate the model and obtain the desired response, refinement of the mesh towards the waterline area is performed as shown in Figure 3.4. The wet surface is defined on the barge as a yellow loading condition shown in Figure 3.5.

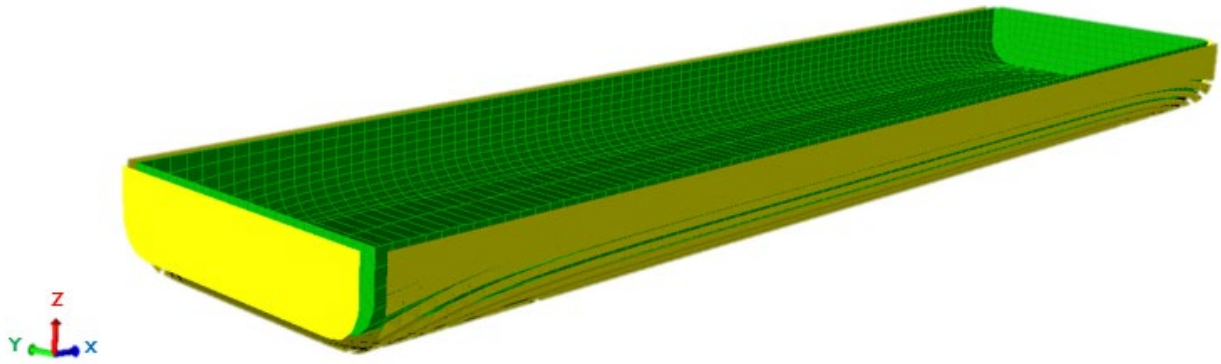

Figure 3.5. Barge hull shown with loading condition applied to the wet surface area in GeniE.

In HydroD, a main Hydromodel is defined as the barge hull. The panel model displayed in Figure 3.2 is placed in the Hydromodel and the waterline is set to 0.185 m. This can be described as the top of the barge hull. Multibody models are made for the different cases and the barge Hydromodel may be translated in Y direction at a desired length to obtain two barges in side-by-side configuration.

Table 3.2. Mesh for the different panel models used in simulations.

Panel Model	Mesh elements	Number of nodes
Barge hull	3720	4385
Internal lid	900	3600
Damping lid 33mm	360	410
Damping lid 66mm	360	410
Damping lid 132mm	360	410

3.1.4 Mass model

While performing a global response analysis, it is possible to create a simple mass model in HydroD, by specifying the total mass, COG and radius of gyration (DNV-GL, 2017). Table 3.3 shows the mass model properties used for the barge Hydromodel. For the validation case, both barges are fixed. This means that the mass model does not affect the result, and vessel motions can be neglected. However, as the investigation continues, the motion of one barge will be released. The floating barge then has to be described with the correct input parameters for mass and bouyancy values to obtain accurate results.

Table 3.3. Mass model properties for the floating barge in HydroD.

Buoyancy volume [m^3]	0.460
Draft of hull [m]	0.185
Total Mass [kg]	462.690
Center of gravity [m]	(0, 0, 0.100)
Center of buoyancy [m]	(0, 0, -0.090)
Radius of gyration [m]	(0.379, 1.160, 1.160)

3.2 Numerical Setup

In Section 2.1.1, the boundary conditions have been explained. In this section, we will look further into the setup behind the artificial damping used in WADAM for the present study. In order to keep the linear dispersion relation, the two parameters introduced for artificial damping will eventually be combined into one single coefficient (Zhao et al., 2018*a*).

Equation (2.6), for the kinematic free surface boundary condition can be simplified as,

$$\Phi_z = \eta_t \tag{3.1}$$

where, η is the water surface and Φ is the velocity potential. Equation (2.7) for dynamic free boundary condition is also simplified to the following form,

$$\Phi_t + g\eta = 0 \tag{3.2}$$

The equations for the kinematic and dynamic free surface boundary conditions can then be combined, and we obtain,

$$\Phi_{tt} + g\Phi_z = 0 \tag{3.3}$$

It is already known that it is possible to introduce a viscous damping effect as in the Newtonian cooling method (Israeli and Orszag, 1981; Kim, 2003). With the dynamic free surface condition as shown in Equation (3.2), the viscous damping effect can be introduced into the linear kinematic free surface condition. Equation (3.1) will then be expressed as,

$$\eta_t = \Phi_z - \mu_1\eta - \frac{\mu_2}{g}\Phi \tag{3.4}$$

In Equation (3.4) the introduced artificial damping terms are expressed as μ_1 and μ_2. It is observed that the introduced viscous damping has a linear form. Next step is to modify the equation for the dynamic free surface condition. Equation (3.2) can be written as:

$$-\frac{1}{g}\Phi_{tt} - \Phi_z - \frac{\mu_1}{g}\Phi_t + \frac{\mu_2}{g}k\Phi = 0 \tag{3.5}$$

Table 3.4. Outputs by re-writing Φ into the form of $\Phi = \varphi e^{i\omega t}$

Input	output
Φ_{tt}	$-\omega^2\Phi$
Φ_t	$i\omega\Phi$
Φ_z	$k\Phi$

By referring to Table 3.4, where k is the wavenumber, Equation (3.5) can then be modified and re-written as,

$$\omega^2 - gk - i\mu_1\omega + \mu_2 = 0 \tag{3.6}$$

Thus,

$$\omega = \pm\sqrt{\left(gk1 - \frac{\mu_2}{gk} - \frac{{\mu_1}^2}{4gk}\right)} + i\frac{\mu_1}{2} \tag{3.7}$$

Now, as we would like to have the linear dispersion relation for the real part of the frequency, it is sufficient to set $4\mu_2 + {\mu_1}^2 = 0$. We observe that μ_2 cannot be positive and Equation (3.4) is expressed as,

$$\eta_t = \Phi_z - 2\varepsilon_1\eta - \frac{\varepsilon_1^2}{g}\Phi \tag{3.8}$$

Referring to Equation (3.8), there are now two damping terms. The first term is used to damp the free surface elevations inside the gap, and the second much smaller term is included to keep the linear dispersion relation unchanged as shown in Equation (3.7).

By combining Equation (3.2) for the dynamic term into Equation (3.8) for the kinematic term, the free surface condition can be written in a time independent expression,

$$\varphi_z = \frac{\varphi}{g}(\omega^2 - i2\varepsilon_1\omega - \varepsilon_1^2) \tag{3.9}$$

The expression can now be simplified by using $\mu = \frac{\varepsilon_1}{\omega}$ and $K = \frac{\omega^2}{g}$. This lead us back to Equation (2.17), and in this case we obtain the expression,

$$\varphi_z = K\varphi(1 - i2\mu - \mu^2) \tag{3.10}$$

Equation (3.10) is only adopted for free surface in the gap. The relationship between the tunable input parameter μ and the non-dimensional damping coefficient used in WADAM is defined as $D = 2\mu$. How these parameters are utilized for the different gap widths will be discussed further in Chapter 4.

Chapter 4

Validation study

The cases for validation are based on a numerical model of two fixed barges subjected to beam sea condition. Experiments have been carried out by Zhao et al. (2017*a*), where a numerical model corresponding to the experiments was developed by Zhao et al. (2018*a*). An illustration of the two fixed barges subjected to beam sea condition is shown in Figure 4.1.

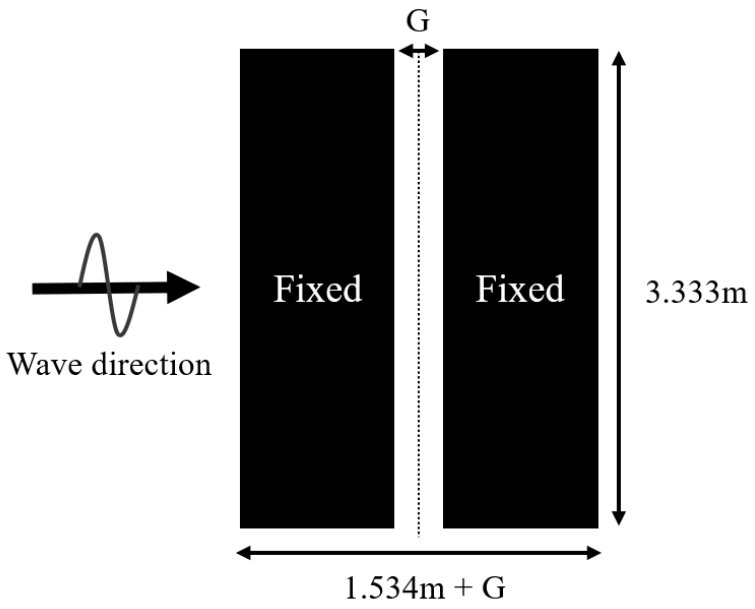

Figure 4.1. Illustration of the two identically fixed side-by-side model scaled barge hulls subjected to a wave direction of 90 degrees, seen from above.

To match the experimental results done by Zhao et al. (2017*a*), Zhao et al. (2018*a*) introduced artificial damping at the free surface of the gap using a numerical model based on three different gap widths. The present study should be validated against the numerical model created by Zhao et al. (2018*a*) to continue the investigation concerning gap resonance coupled to vessel motions.

The numerical simulations are carried out by using three different gap widths set to a scale of 1:60. The largest *G* value is 132 mm, corresponding to 8 m at full scale. The second and third *G* values are 66 mm and 33 mm, corresponding to 4 m and 2 m at full scale. The damping coefficient $D = 2\mu$ changes with *G*, and the relationship between input and damping parameters can be seen in Table 4.1.

Table 4.1. relationship between Input and damping parameters for different gap widths, G.

G = 132mm		G = 66mm		G = 33mm	
Input parameter	Damping coefficient	Input parameter	Damping coefficient	Input parameter	Damping coefficient
μ	D	μ	D	μ	D
0.0025	0.0050	0.0048	0.0096	0.0068	0.0136

By running numerical simulations, surface elevations in three different gap widths are obtained based on off-body-points placed in the gap center. The methodology describing how the RAOs of the gap resonance can be computed using potential flow theory is shown in Section 2.1. The panel models used to model the hull and free surface are shown in Section 3.1.3. The present numerical results without additional artificial damping are shown in Figure 4.2, Figure 4.3 and Figure 4.4, for different gap widths, respectively. The blue solid curve refers to the present numerical results, whereas the red stapled curve refers to the numerical results done in Zhao et al. (2018*a*). It is important to denote that the results in these figures are undamped calculations of the gap resonant response. The numerical results based on the present model agrees very well with the numerical results obtained by Zhao et al. (2018*a*). Minor differences can be seen in Figure 4.4 for the $m = 9$ peak.

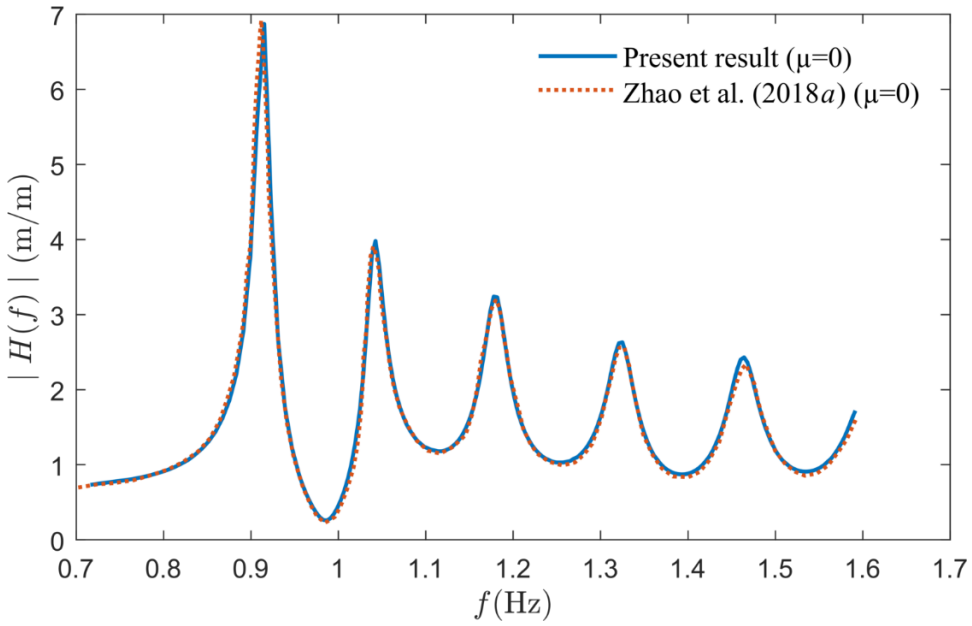

Figure 4.2. Comparison of the numerical results of the gap resonance for G = 132 mm.

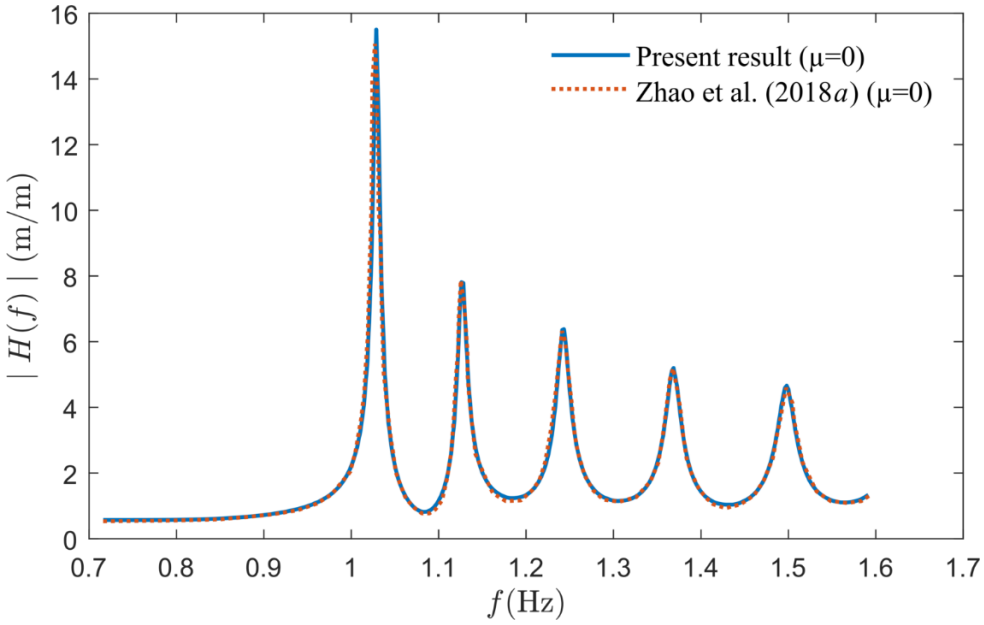

Figure 4.3. Comparison of the numerical results of the gap resonance for G = 66 mm.

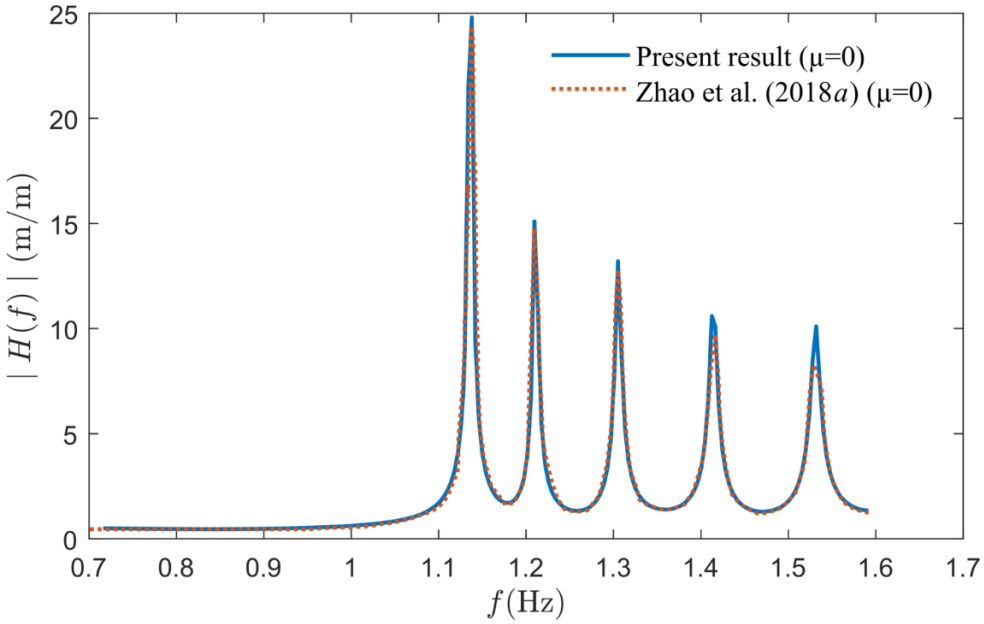

Figure 4.4. Comparison of the undamped numerical results of the gap resonance for G = 33 mm.

By neglecting the additional viscous damping contributions, the only damping is due to waves radiated to infinity. The calculated gap RAOs then tend to infinity as *G* goes to zero and can clearly be seen in the results as *G* decreases. Nonetheless, Zhao et al. (2018*b*) reported that the experimental data indicate that there is a value of G giving the maximum amplitude for the gap resonance amplitude.

Based on the numerical results obtained by Zhao et al. (2018*a*), it is known that the agreement to the experimental results reported by Zhao et al. (2017*a*) is less satisfactory for the narrowest gap (*G* = 33 mm). As the gap width gets extremely small, viscous damping becomes more important than potential flow radiation damping. In order to improve the agreement between the potential flow theory calculations and experimental data, appropriate damping coefficients at the different gap resonant modes have been introduced. The additional damping is linear and is applicable in this case because the viscous damping of the gap resonance can be a result of Stokes laminar boundary layers, where the damping is linear (Zhao et al., 2017*a*, 2018*b*). By considering the case in full scale, the viscous boundary layer characteristics may be in a different regime. Nevertheless, the upper estimates of the gap resonant responses are most likely to be carried through when scaled up to a realistic case.

As the linear potential flow calculations overpredicts the gap resonant response, artificial damping is applied to the various gap widths as defined in Table 4.1. An important observation is that the gap width is reduced as the resonant response increases; hence, the artificial damping term is larger for narrower gaps. By applying artificial damping to the free surface of the gap, Zhao et al. (2018*a*) found the calculated RAOs of the free surface elevations to agree very well with the experimental results reported by Zhao et al. (2017*a*).

As the model has now been validated through validation study, the artificial damping is applied to the different gaps based on the information given in Table 4.1. In Figure 4.5, Figure 4.6 and Figure 4.7, comparisons of the previous numerical results by Zhao et al. (2018*a*) are plotted against the present numerical results for three different gap widths. The same artificial damping coefficients are applied to the new numerical model and the predicted results agree well with the numerical damped results reported by Zhao et al. (2018*a*). The yellow dashed line refers to the produced results using the present model, whereas the green dash-dotted line refers to the damped numerical results made by Zhao et al. (2018*a*).

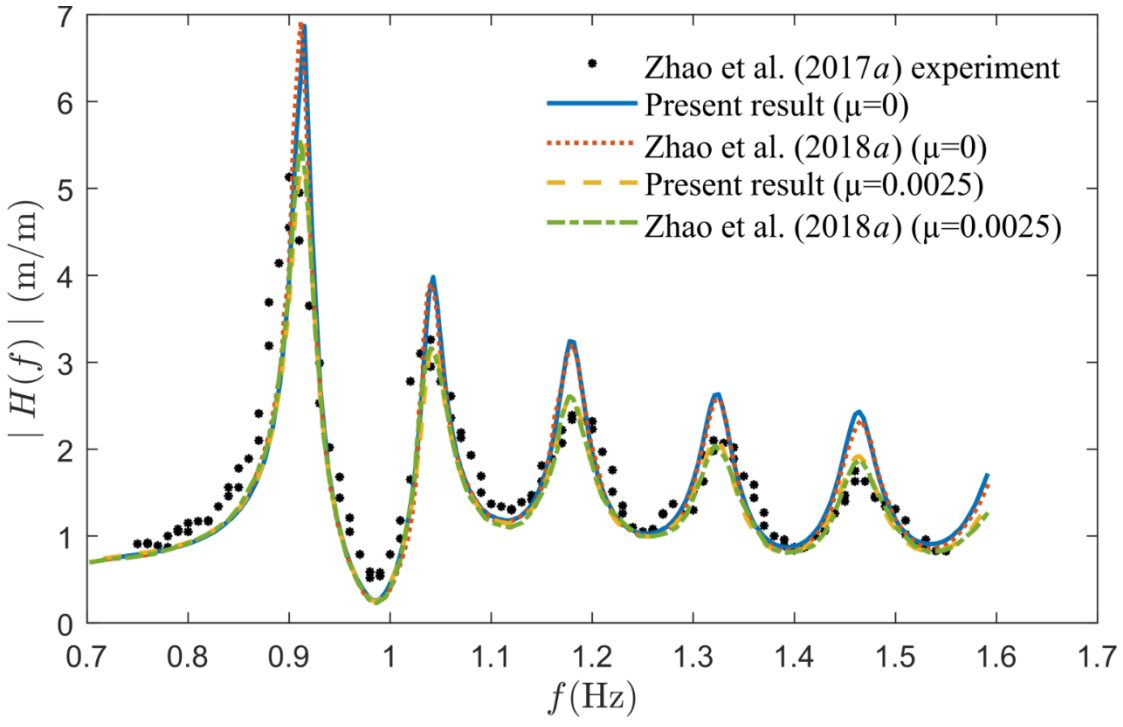

Figure 4.5. Comparison of experimental data plotted against both damped and undamped numerical results of the gap resonance for G = 132 mm.

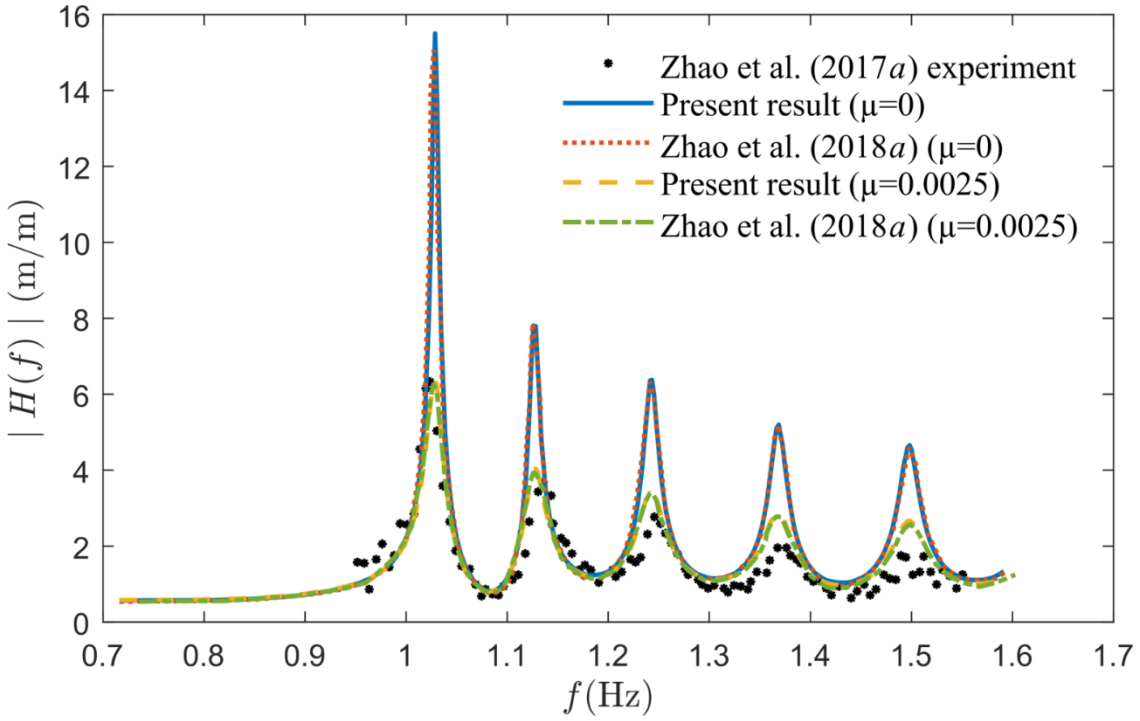

Figure 4.6. Comparison of experimental data plotted against both damped and undamped numerical results of the gap resonance for G = 66 mm.

The two largest gaps (4 m and 8 m in full scale), are the most realistic cases and will be used for further investigation in this thesis. For the extremely narrow gap case (2 m in full scale), more artificial damping is needed to damp the higher gap resonant modes.

In order to provide reasonable results during the present validation study, an important factor turned out to be the panel mesh density at the water surface, where the boundary element method states that 5 panels over a wavelength should be enough. Furthermore, it also states that a panel density larger than 12 per wavelength should be enough to provide convergence. The numerical results reported by Zhao et al. (2018*a*) converged and so does the numerical results for the present model.

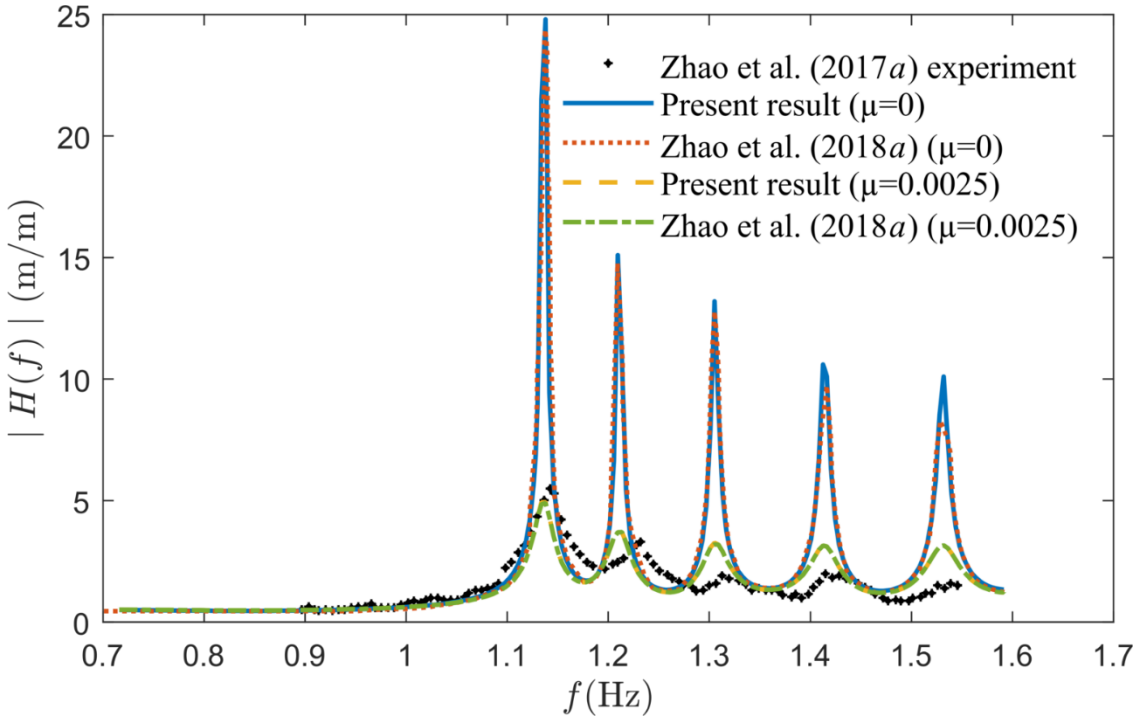

Figure 4.7. Comparison of experimental data plotted against both damped and undamped numerical results of the gap resonance for G = 33 mm.

Chapter 5

Coupling between Vessel Motions and Gap Resonance

The gap resonance phenomenon in the fluid between two fixed barges has been presented and discussed in Chapter 4. In this chapter, the coupling effects between ship motions and gap resonances are investigated. For comparison, the behavior of a single floating barge is analyzed before it is introduced in side-by-side configuration. To examine the motion performance of the barge, the mass properties are important. The simulations are again conducted using DNV-GL Sesam software. Hydrodynamic analysis is done through HydroD and a series of numerical simulations based on the linear potential flow solver WADAM.

5.1 A single floating barge

The directions of the input waves with respect to the vessel are given in Figure 5.1.

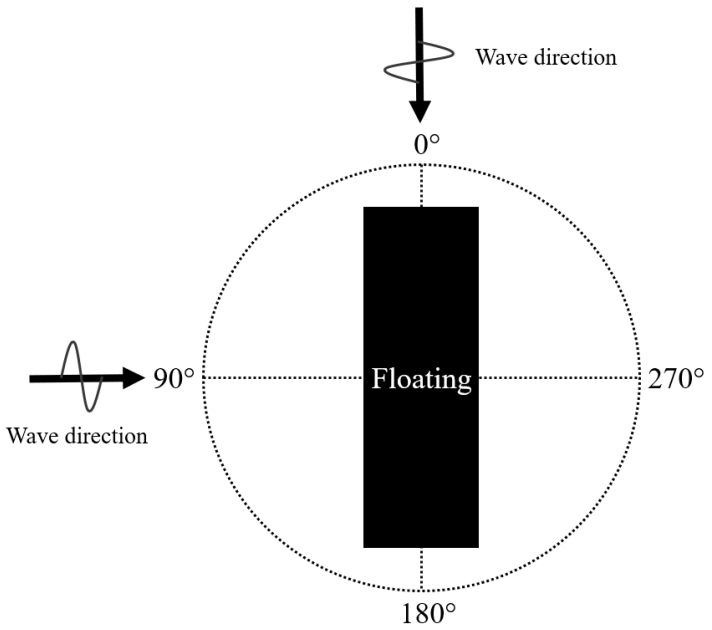

Figure 5.1. Definition of the wave directions, a top view.

5.1.1 Roll motions of a single floating barge

Based on the inertial parameters provided in Table 5.1, the natural period of the barge roll motion is estimated to be 15 s at full scale, corresponding to approximately 2 s at a model scale of 1:60. The input parameters are further used to calculate the RAO of the floating barge in 6 degrees-of-freedom (DOFs). Figure 5.2 illustrates the case subjected to 90 degrees wave direction.

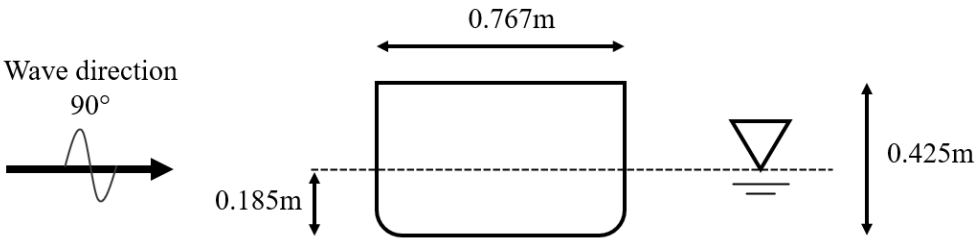

Figure 5.2. Configuration of the numerical model for waves approaching from 90º.

Table 5.1. Mass model properties for the floating barge.

Buoyancy volume [m^3]	0.460
Draft of hull [m]	0.185
Total Mass [kg]	462.690
Center of gravity [m]	(0, 0, 0.100)
Center of buoyancy [m]	(0, 0, -0.090)
Radius of gyration [m]	(0.379, 1.160, 1.160)

It is well known that the potential flow code ignores the viscous damping in the calculation, but the viscous damping plays an important role in the estimation of ship motions in particular for the roll motions (Zhao et al., 2016; Zhao et al., 2017*b*). It is therefore necessary to include the effect of viscous damping. The viscous damping is usually considered through a term which is expressed as a coefficient of critical damping. By using this approach, we may find the damping value to compensate for the viscous damping lost in the potential flow calculation and with that achieve the desired roll motion.

In order to simulate the motions of the barge correctly, a sensitivity analysis using different sets of critical damping is performed. Without the critical damping, the only damping is radiation damping, which is frequency dependent. By including the different sets of critical damping for the roll motion of the barge, the damping term of the equation of motion changes and we can obtain a more realistic behavior.

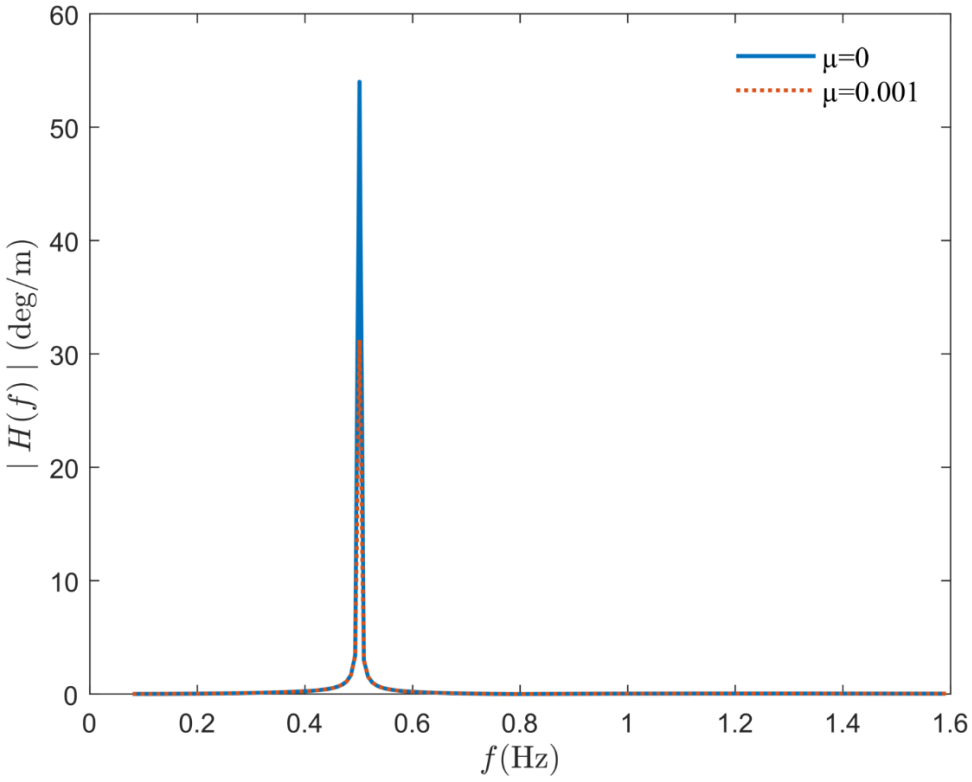

Figure 5.3. Roll RAOs for a single floating barge subjected to a wave direction of 90°.

As shown in Figure 5.3, the roll RAO is unrealistically large without any viscous damping applied. The blue curve represents the single floating barge without any critical damping whilst the red curve has 0.1% critical damping applied. It is worth mentioning that these roll RAOs are given based on a unit amplitude wave, e.g. a unit amplitude wave may induce 55^{o} roll motion if there is no viscous damping. By including only, a small amount of critical damping, the magnitude of the RAO is reduced by half. As 0.1% of critical damping is still not big enough to make a realistic roll motion for the barge, further cases are analyzed.

Figure 5.4 compares the roll RAOs with different levels of critical damping being applied to the roll motion. The green curve where 3% critical damping is applied seems to be satisfactory to damp the roll motion and thus will be included for the rest of the study. It is worth noting that the exact critical damping coefficient is not important here, though it can be determined through CFD simulations, or model tests, as we are focusing on coupling between gap resonance and vessel motions. As long as the ship motions are realistic (or close to), they will not affect our analysis of the coupling between the ship motions and gap resonance.

To better understand the roll motion, the phase information is plotted in Figure 5.5. At the resonant frequency, it should be possible to see a significant phase change. By looking at Figure 5.5, at the natural period of roll, the phase change is observed.

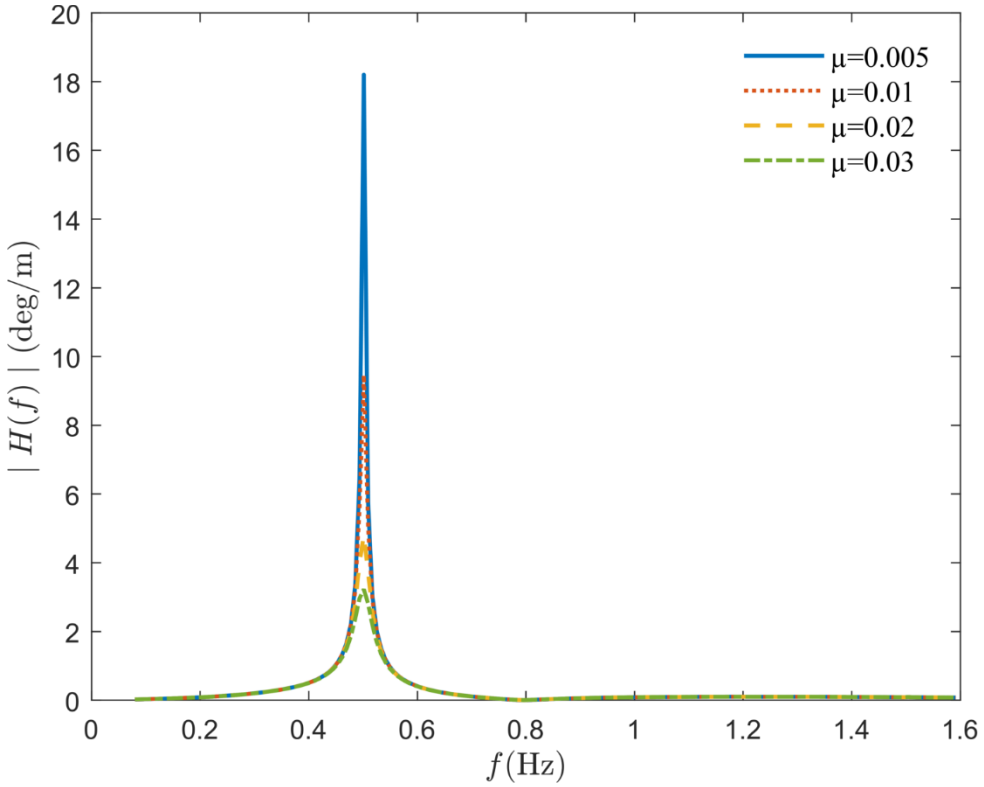

Figure 5.4. Effects of viscous damping on the roll RAOs for a floating barge subjected to a wave direction of 90deg.

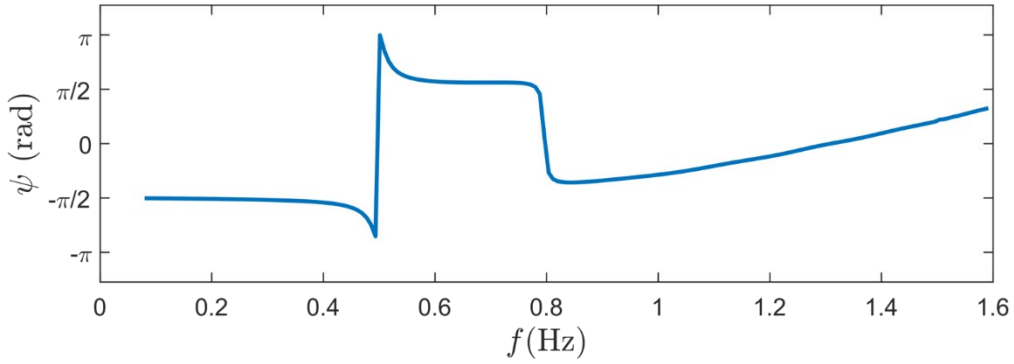

Figure 5.5. Phase information of the roll motion of the single floating barge subjected to waves from 90°.

5.1.2 Pitch motions of a single floating barge

The pitch for the floating barge is calculated by changing the wave direction to 0°, making the barge subjected to head waves. An illustration of the case can be seen in Figure 5.6, and the calculated pitch RAO is displayed in Figure 5.7. As the radiation damping in pitch is large while the viscous damping is small, applying critical damping is not as important as for the roll motion. Thus, no additional viscous damping is considered for pitch motion.

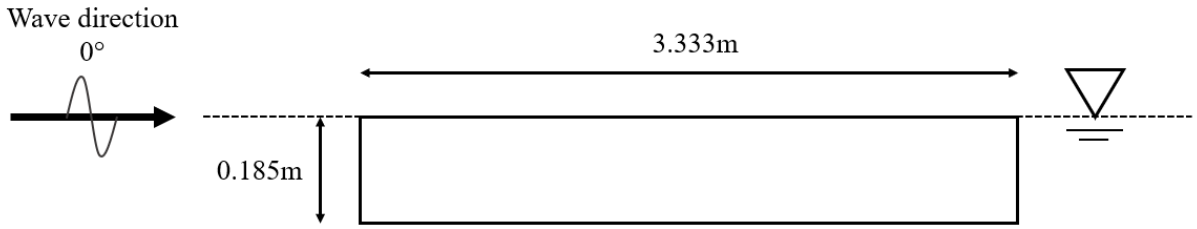

Figure 5.6. Illustration of the barge subjected to head waves, seen from 90 degrees.

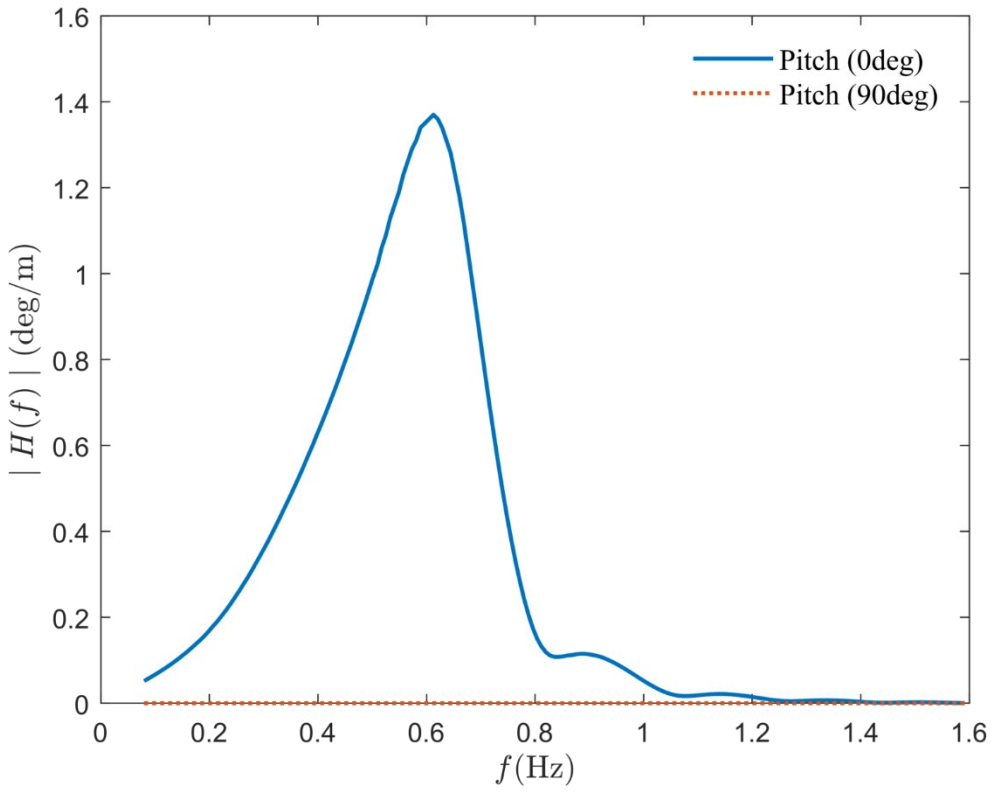

Figure 5.7. Pitch RAO for a single floating barge subjected to wave directions of 0 and 90 degrees.

5.1.3 Heave- single floating barge

Figure 5.8 shows the RAOs for the heave motion of the vessel, showing a peak at f = 0.76 Hz. It can also be seen that the RAOs tend to unity at low frequency, as the barge moves uniformly with the associated sea condition. However, as the frequency tends to be infinite, the RAO becomes zero.

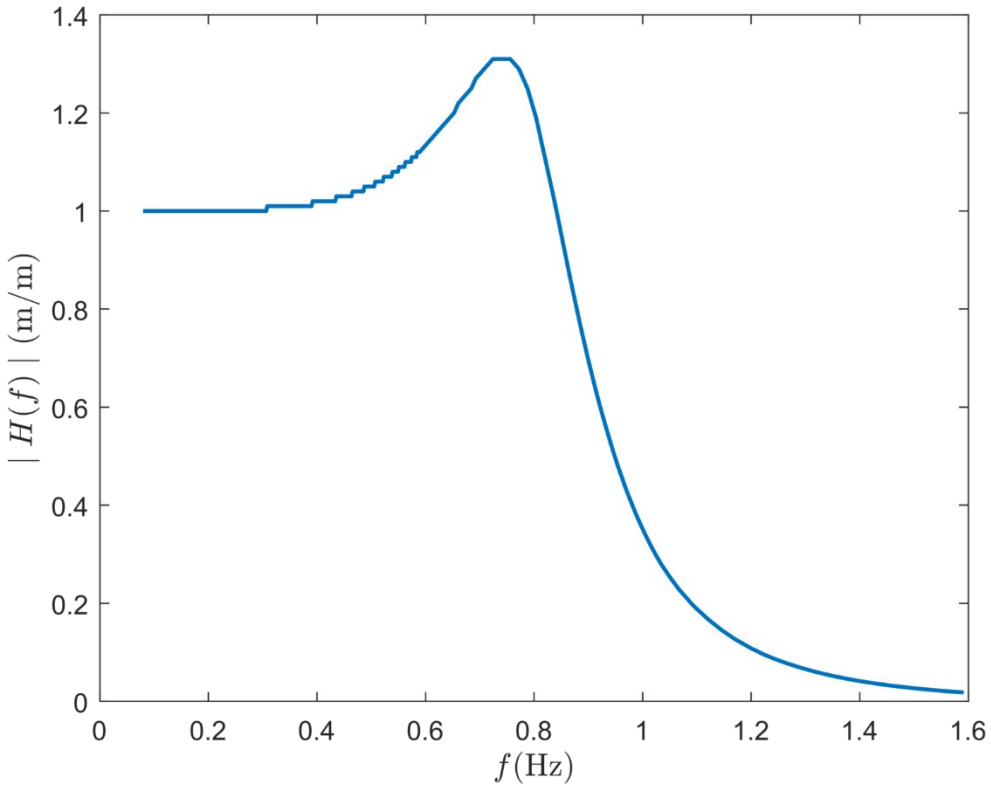

Figure 5.8. RAO in heave for the floating barge subjected to a wave direction of 90°.

5.2 Gap resonance in between a fixed and a floating barge

As the motion of the single barge has been carried out, the investigation continues by looking at two barges in side-by-side configuration, forming a narrow gap in between. The gap resonance in between two fixed barges has been investigated in Chapter 4. Here we release the motion of one barge, to explore the effects of vessel motions. The two identical barges are subjected to different sets of wave directions through various simulations. An illustration of the case can be seen in Figure 5.9. The gap width G has been set to 66 mm for the entire process. Surface elevation is measured in the center of the gap at the orange point marked as WG.

5.2.1 Gap center- beam sea

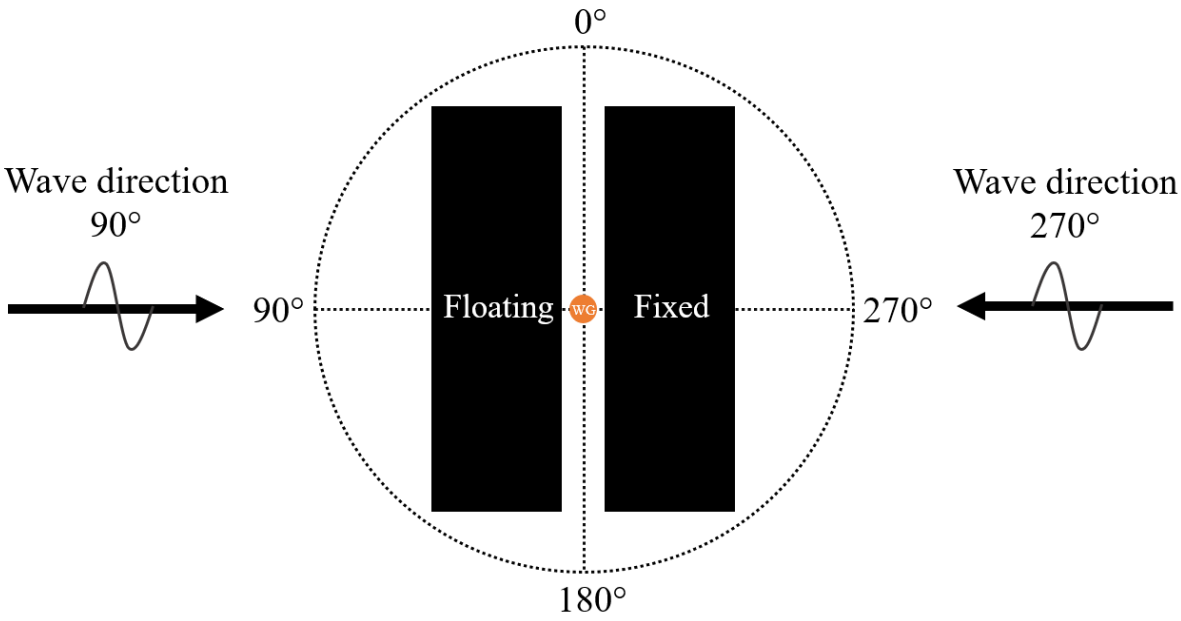

Figure 5.9. Illustration of the two barges subjected to different sets of wave directions, seen from above.

The gap resonances measured in the center of the gap are given in Figure 5.10, for three different configurations, i.e. (1) both barges fixed, (2) one floating barge plus one fixed barge, and (3) two barges floating.

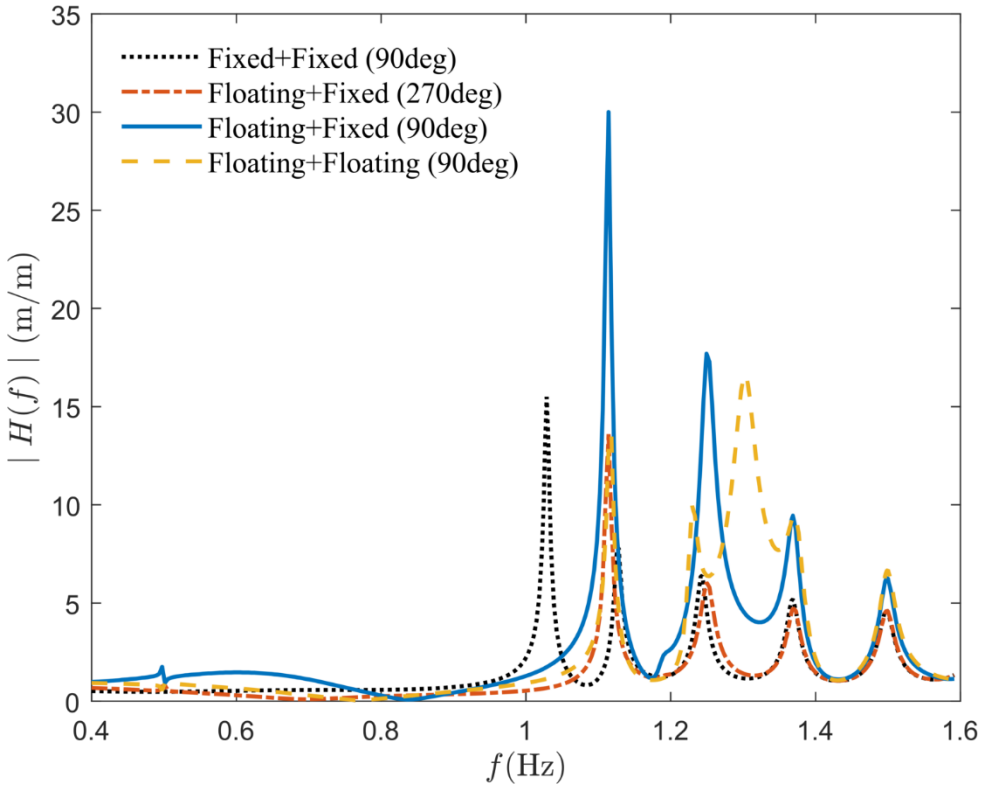

Figure 5.10. Comparison of the surface elevations in the middle of the gap plotted against frequency, where G = 66 mm.

There is a small response peak in the gap resonant RAOs at frequency around 0.5 Hz, which is due to the coupling effect from the roll motion. However, the peak amplitude is very small compared to the main peaks. This suggests that the coupling between roll motion and the gap resonances is weak, at least from the linear analysis.

The most striking observation in Figure 5.10 is that the first gap mode disappears when the barge motions are released – either one of the barges or both, while the frequency of the second RAO peak, the $m = 3$ mode (see Zhao et al. 2017*a* and Section 2.4.1 for mode description), is slightly shifted towards lower frequency. As moving further away from the $m = 1$ mode, the effect of the

ship motion is less important. Interestingly, the RAOs are significantly increased when one of the barge motions are released. When both barges are floating, there are more gap modes excited.

The highest response is observed in the case where the waves approach the barges with 90° incident angle. As this is the case where the exposed barge is floating, a higher impact is reasonable regarding the case where the exposed barge is fixed.

As the frequency gets higher, the three cases become more and more alike. It is noted that there is no viscous damping applied to the gap surface. Figure 5.11 shows the phase angles for the two different wave directions. Each vibration in Figure 5.11 can be connected to the significant phase changes for the different cases in Figure 5.10.

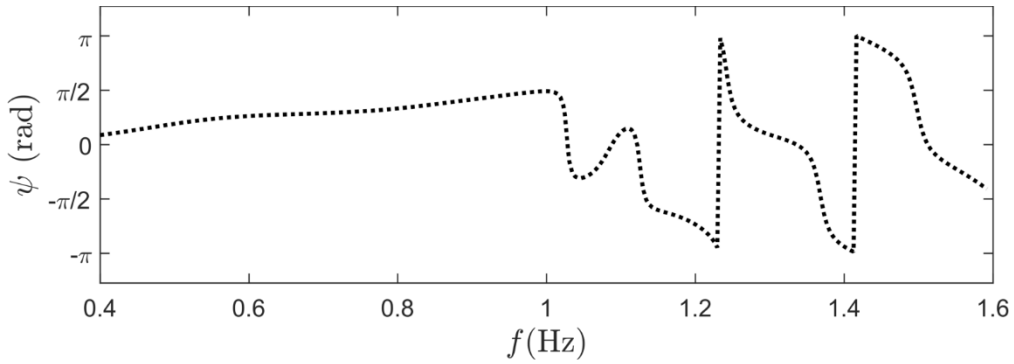

(a)

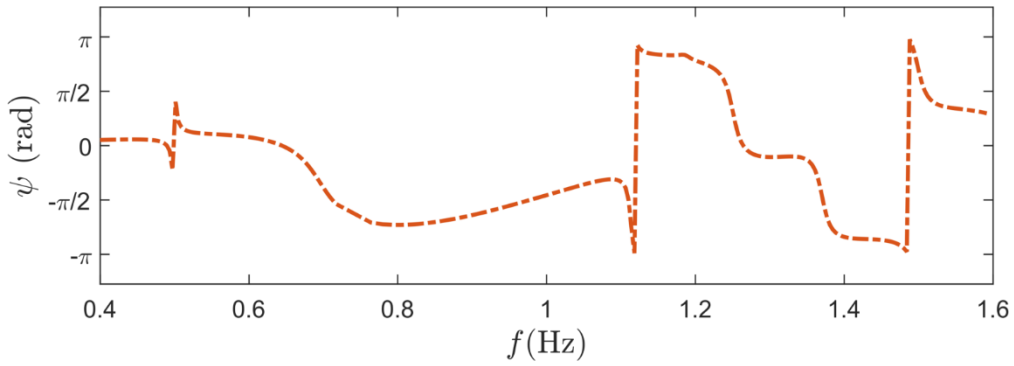

(b)

Figure 5.11. Values for phase angles in the middle of the gap for (a), two fixed barges in beam sea, (b) one fixed and one floating barge subjected to 270° beam sea, (c), one fixed and one floating barge subjected to 90° beam sea, and (d), two floating barges in beam sea.

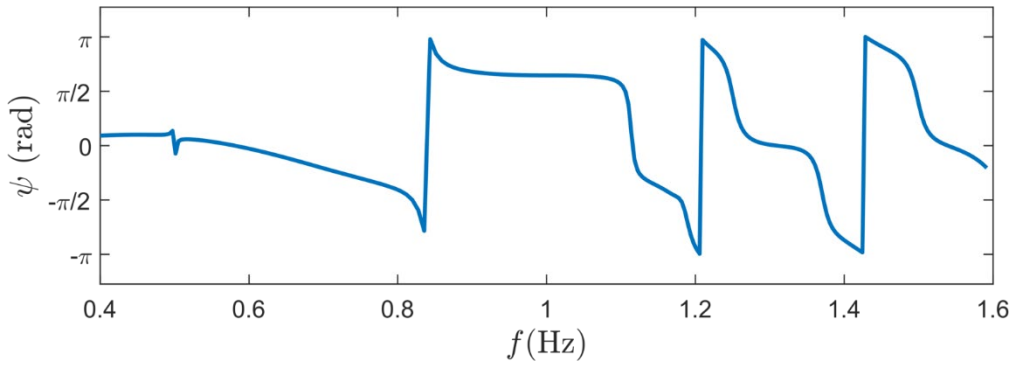

(c)

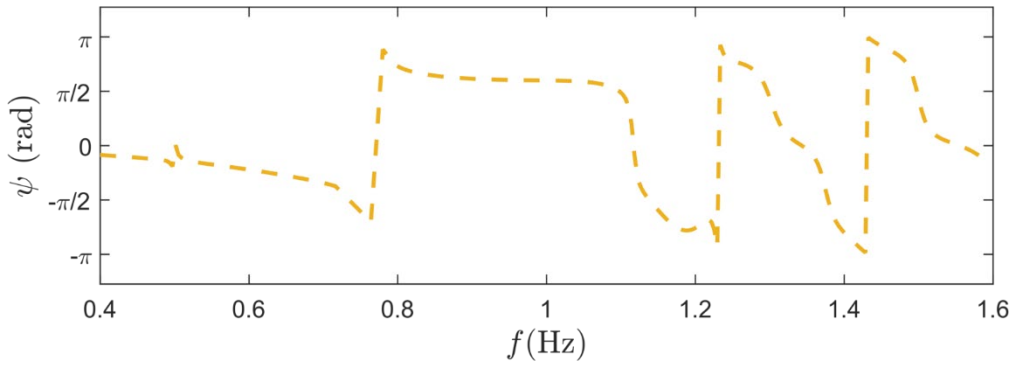

(d)

Figure 5.11. Continued.

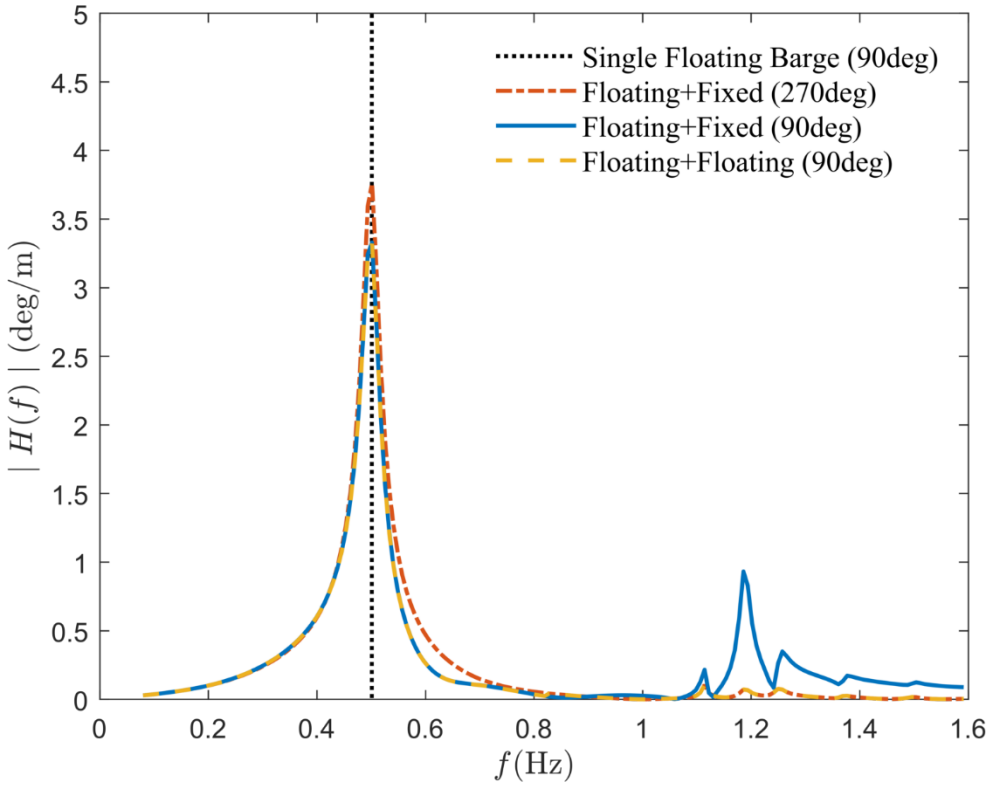

Figure 5.12. Roll RAOs of the floating barge with the same configuration as in Figure 5.9.

As displayed in Figure 5.12, the black dotted line refers to the highest crossing between the single barge and the combined case. It is interesting to see that the RAO peak with 270 degree incident angle is larger than that in the 90 degree case. It is also observed that the 90 degrees wave direction results in additional peaks smaller than the main roll peak. The additional roll peaks are relevant to the gap resonance modes as observed in Figure 5.10. As discussed above, in Figure 5.10, a small effect can be observed around $f = 0.5$ Hz. This can be described as a coupling effect from the vessel motion as the roll natural period from Figure 5.12 is also at $f = 0.5$ Hz.

Furthermore, Figure 5.13 show that there are some heave RAO peaks around the frequencies of gap modes, which is not surprising and is a result of the gap resonant effects. From 270 degrees wave direction, the floating barge is protected by the fixed barge, leading to a weaker heave response. It can also be seen that the magnitude of the heave RAO is larger for the floating barge in side-by-side configuration from 90 degree wave direction, than the single floating barge.

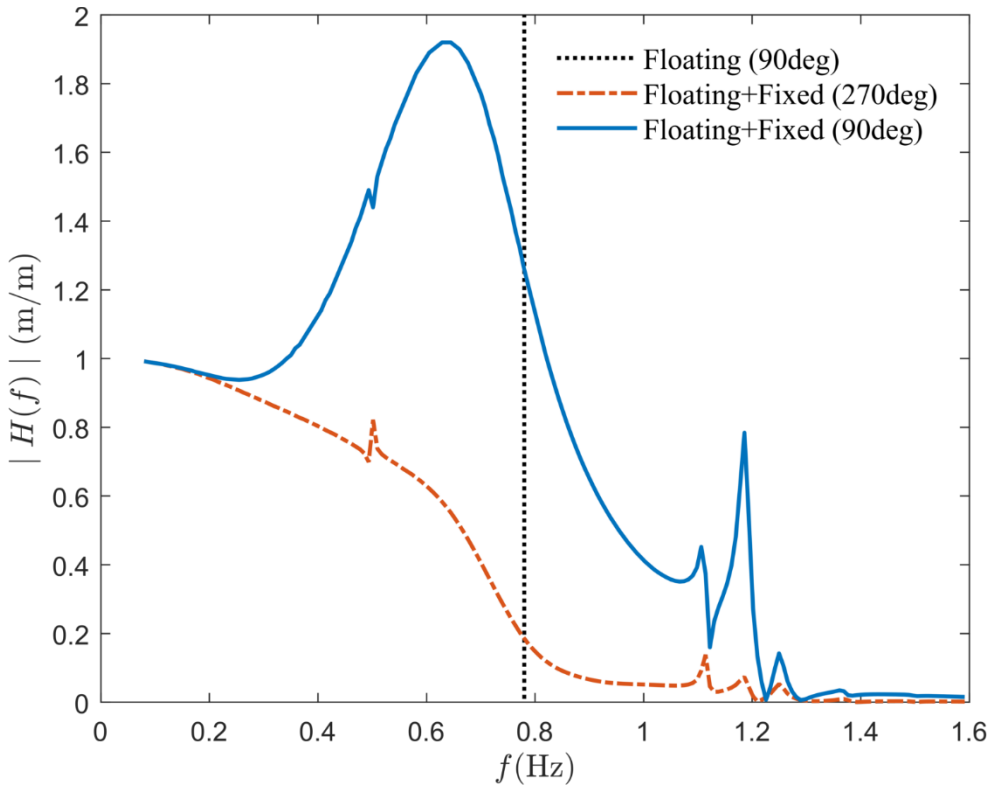

Figure 5.13. Comparison of the heave motion of the floating barge, while having a configuration as shown in Figure 5.9. The black dotted line refers to the highest crossing between the single floating barge and the combined case.

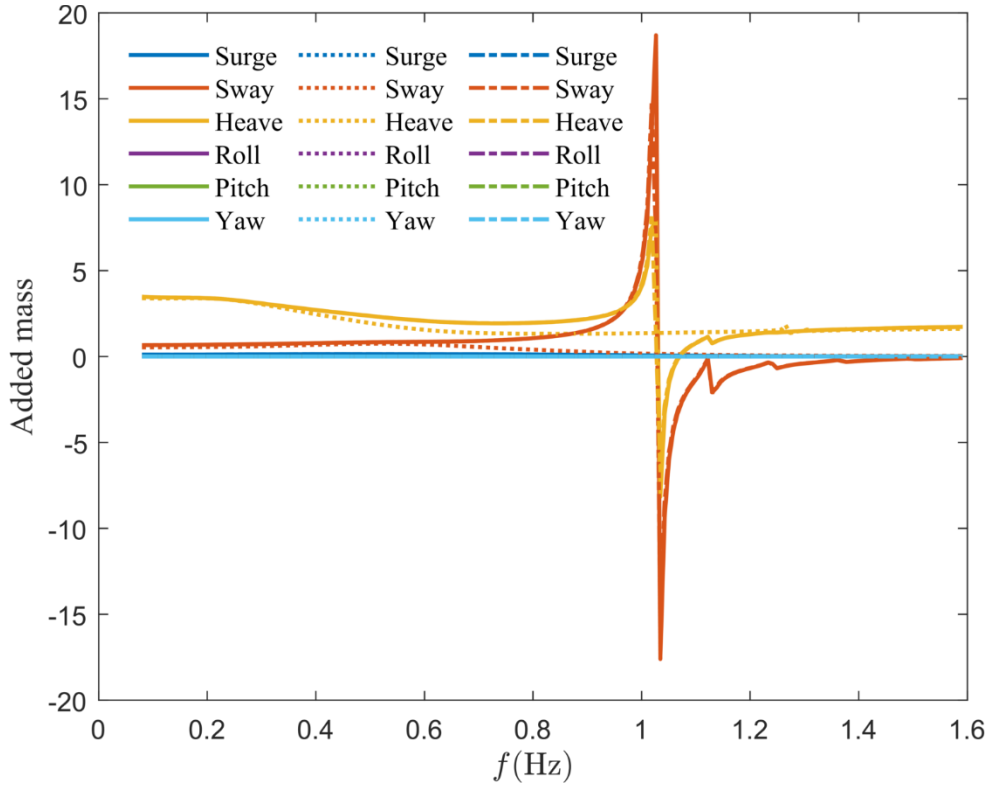

Figure 5.14. Added mass coefficients of the floating barge. The solid curves represent the added mass of the floating barge in side-by-side configuration with one floating and another fixed, the dotted curves represent a single floating barge, and the dash-dot curves for the case in the two floating configuration.

To explore the reason of the disappearance of the first mode in the gap surface elevation from Figure 5.10, added mass and damping coefficients are investigated. As shown in Figure 5.14, the added mass for the sway and heave motions is changed significantly. The disappearance of the first mode in the gap surface elevation have previously been reported by Sun et al. (2015), where two floating barges also resulted in the disappearance of the first gap mode response. The frequency $f = 1.03$ Hz where significant change of heave and sway occurs is the same as that of the first gap mode. The coupling between sway and heave motion together with the $m = 1$ mode seems to have cancelled the first mode response. It is worth noting that the roll motion also shows some sudden change at the frequency $f = 1.03$ Hz, but the absolute value of roll is so small, e.g. 10^{-6}, that its effect is negligible.

Furthermore, we plot the radiation damping coefficients in Figure 5.15, where the one can observe changes at frequency of $f = 1.03$ Hz, for the sway, heave and roll motions. However, the radiation damping for roll is much smaller compared to that for sway and heave.

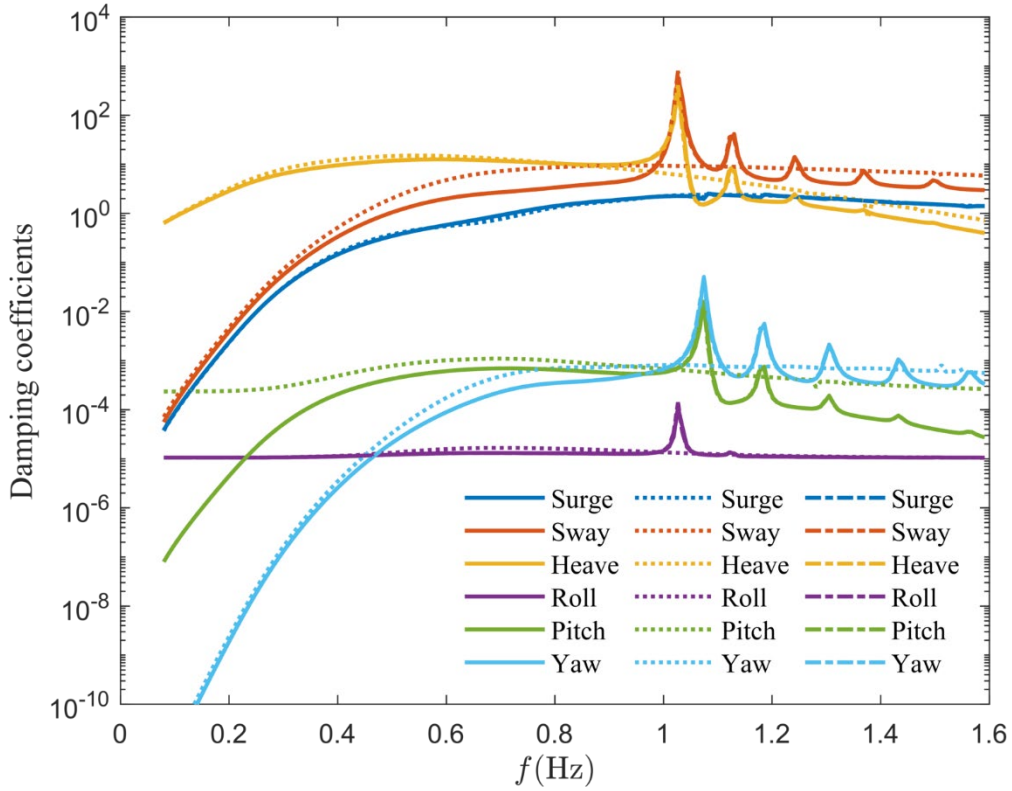

Figure 5.15. Damping coefficients of the floating barge. The solid curves represent the added mass of the floating barge in side-by-side configuration with one floating and another fixed, the dotted curves represent a single floating barge, and the dash-dot curves for the case in the two floating configuration.

5.2.2 Gap center- head sea

To observe the effects of head waves in the gap, a wave direction of 0 degree is applied, as shown in Figure 5.16. The orange measuring point marked as WG is still in the centre of the gap, and the gapwith *G* is still 66mm.

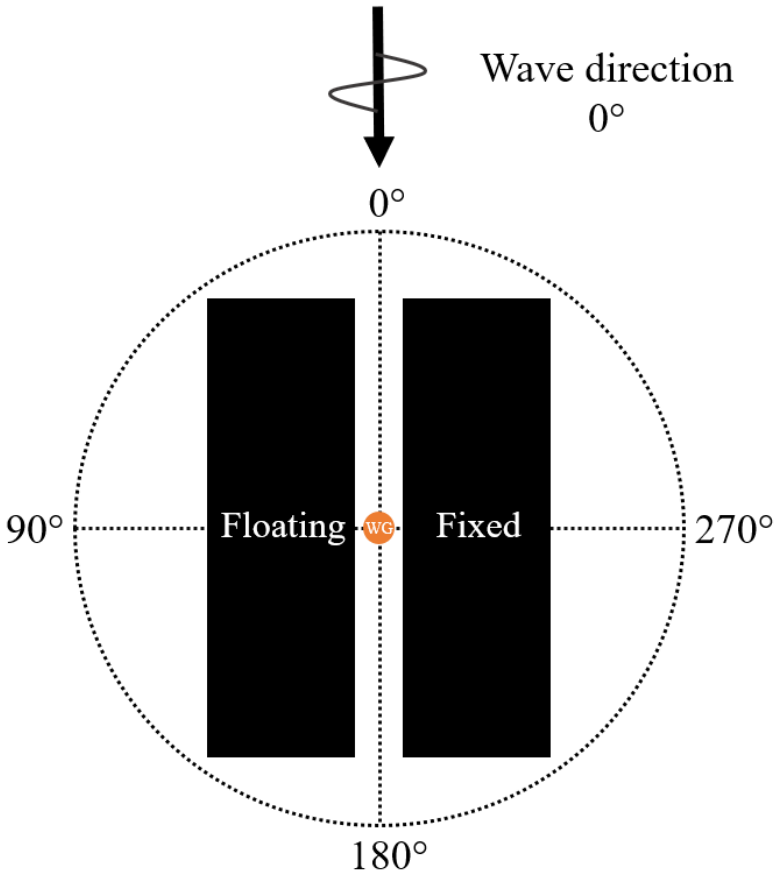

Figure 5.16. Illustration of the two barges subjected to head waves at 0°, seen from above.

The gap resonances measured in the center of the gap are given in Figure 5.17, for three different configurations, i.e. (1) both barges fixed, (2) one floating barge plus one fixed barge, and (3) two barges floating. A small response peak in the gap resonant RAOs can be seen at frequency around 0.5 Hz, which is due to the coupling effect with pitch motion. Again, the peak amplitude is very

small compared to the main peaks. Thus, it suggests that the coupling between pitch motion and the gap resonance is weak from the linear analysis. Similar observations compared to the beam sea case in Figure 5.10 can be seen as the first gap mode disappears when the barge motions are released. The frequency of the $m = 3$ mode is slightly shifted towards lower frequencies. As the frequency increases, all the cases become more and more alike. In contrast to the beam sea case, here only the $m = 3$ mode has higher magnitude than the other modes when the barge motions are released. When both barges are floating, again more gap modes are excited. It should be noted that no viscous damping has been added to the gap surface.

For the phase angles, the same applies for head sea as for the beam sea. Each vibration in Figure 5.17 can be connected to a significant phase change in Figure 5.18.

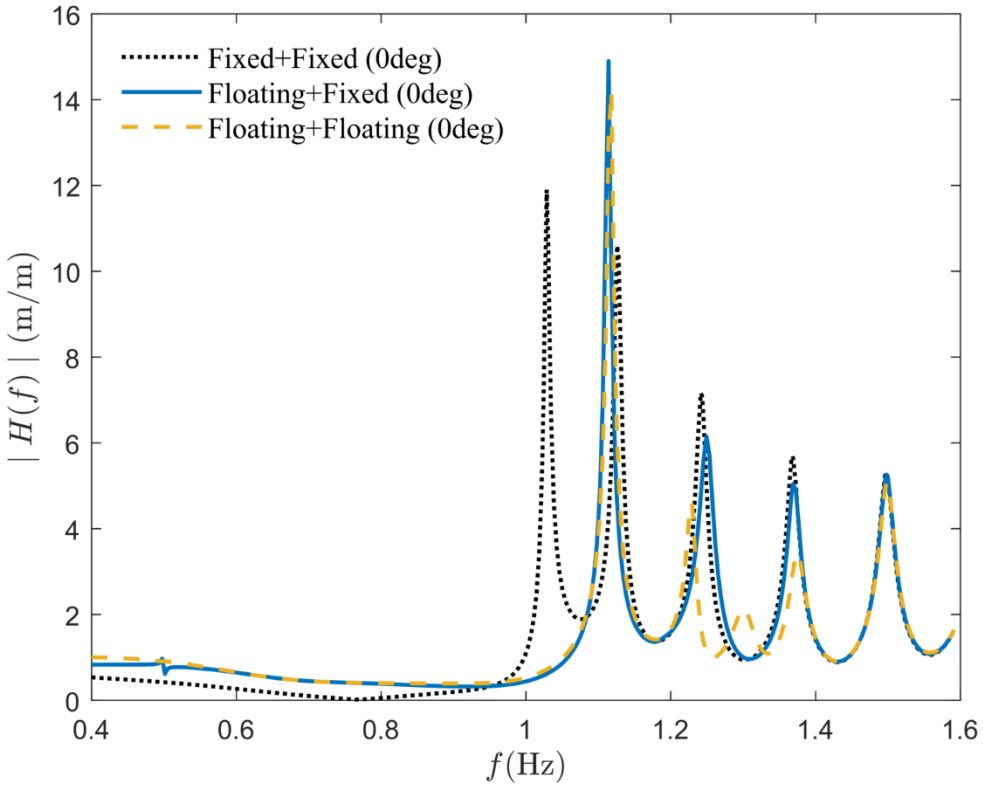

Figure 5.17. Comparison of the surface elevation in the middle of the gap, having a configuration as shown in Figure 5.16.

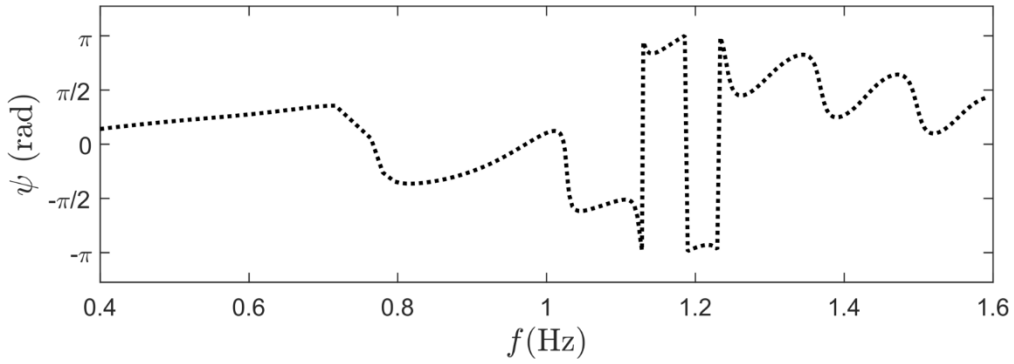

(a)

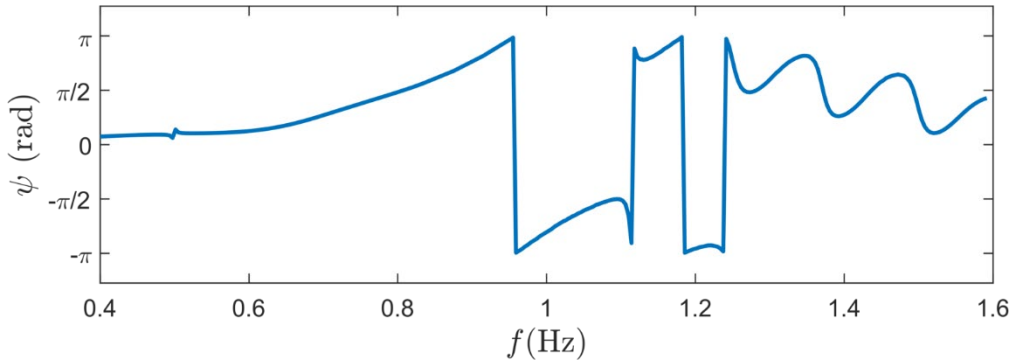

(b)

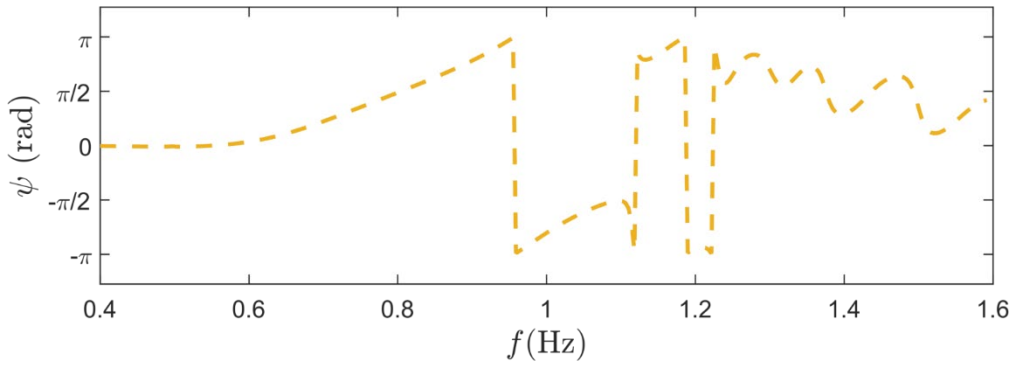

(c)

Figure 5.18. Values for phase angles in the middle of the gap in head waves for (a) two fixed barges, (b) one fixed and one floating barge and (c), two floating barges.

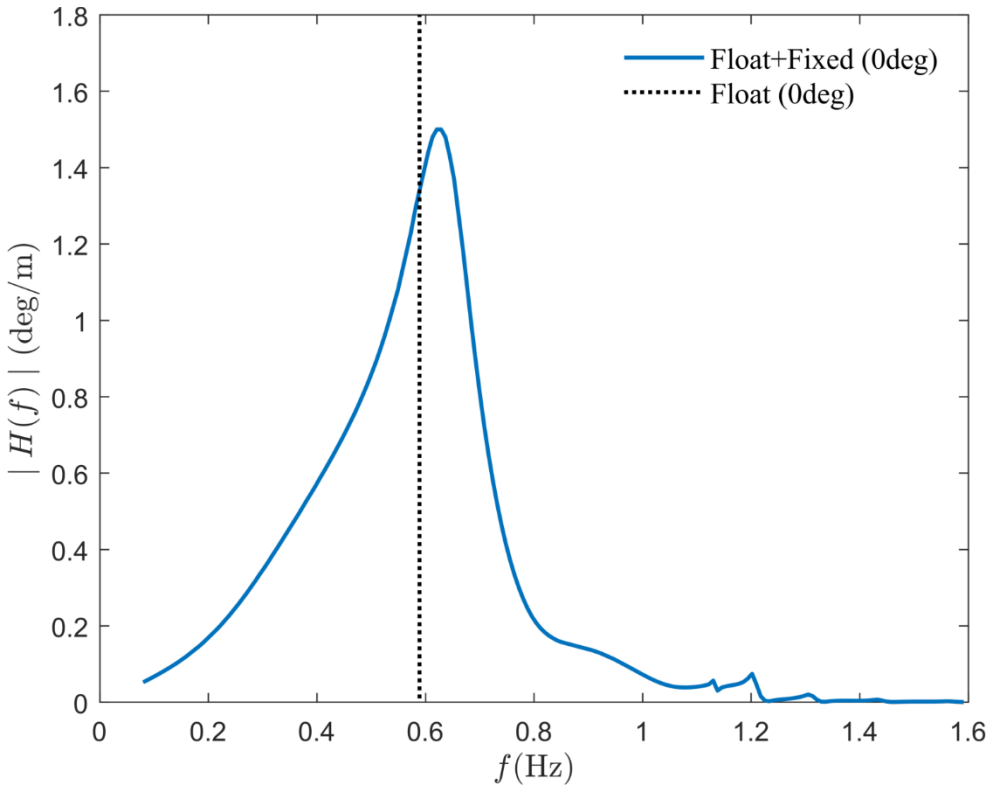

Figure 5.19. Pitch motion of the floating barge while having a configuration as shown in Figure 5.16.

The black dotted line in Figure 5.19 refers to natural frequency of pitch motion for a single floating barge. It seems like the natural frequency is shifted towards higher frequency due to the presence of the fixed barge.

Furthermore, regarding the added mass and damping coefficients, the same discussion holds for the head sea condition as discussed in the beam sea condition. To give the reader a clear perspective, Figure 5.20 for the added mass coefficients, and Figure 5.21 for the damping coefficients are shown below.

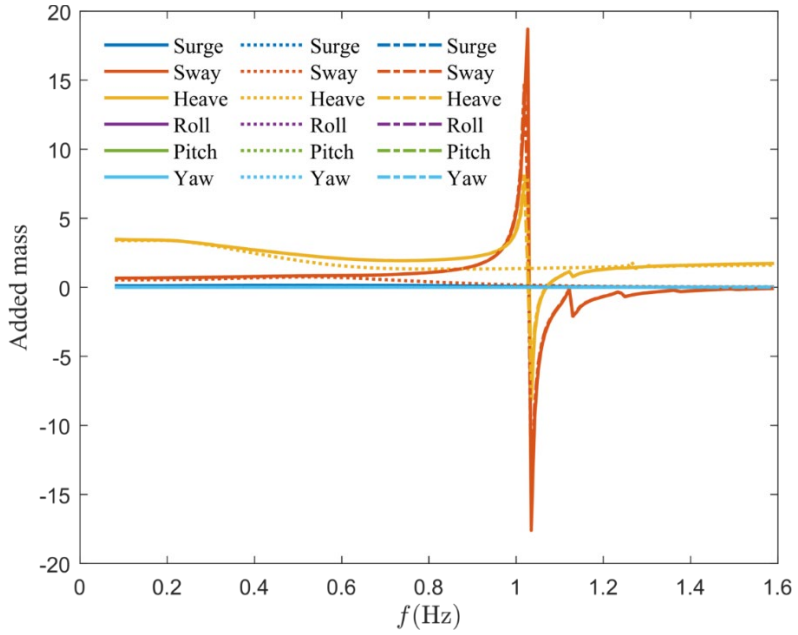

Figure 5.20. Added mass coefficients of the floating barge. The solid curves represent the added mass of the floating barge in side-by-side configuration with one floating and another fixed, the dotted curves represent a single floating barge, and the dash-dot curves for the case in the two floating configuration.

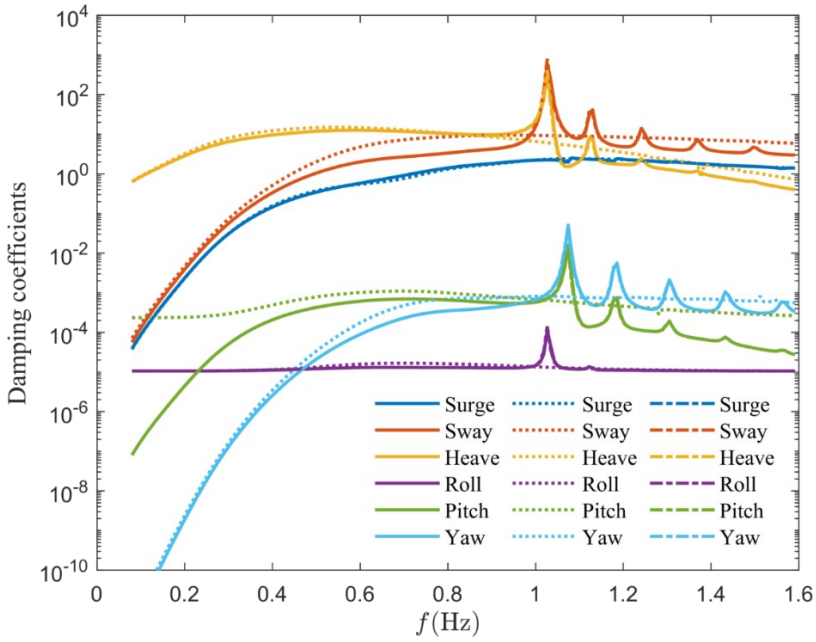

Figure 5.21. Damping coefficients of the floating barge. The solid curves represent the added mass of the floating barge in side-by-side configuration with one floating and another fixed, the dotted curves represent a single floating barge, and the dash-dot curves for the case in the two floating configuration.

5.3 Influence of gap width and artificial damping

5.3.1 Two fixed barges

The numerical results in this section is still based on the model scaled case. However, the gap widths are given in full scale in the figure legends to give readers more direct expressions. Figure 5.22 suggests that, the amplitude of $m = 1$ decreases significantly as the gap width increases. In contrast, the natural frequency shifts towards lower frequency.

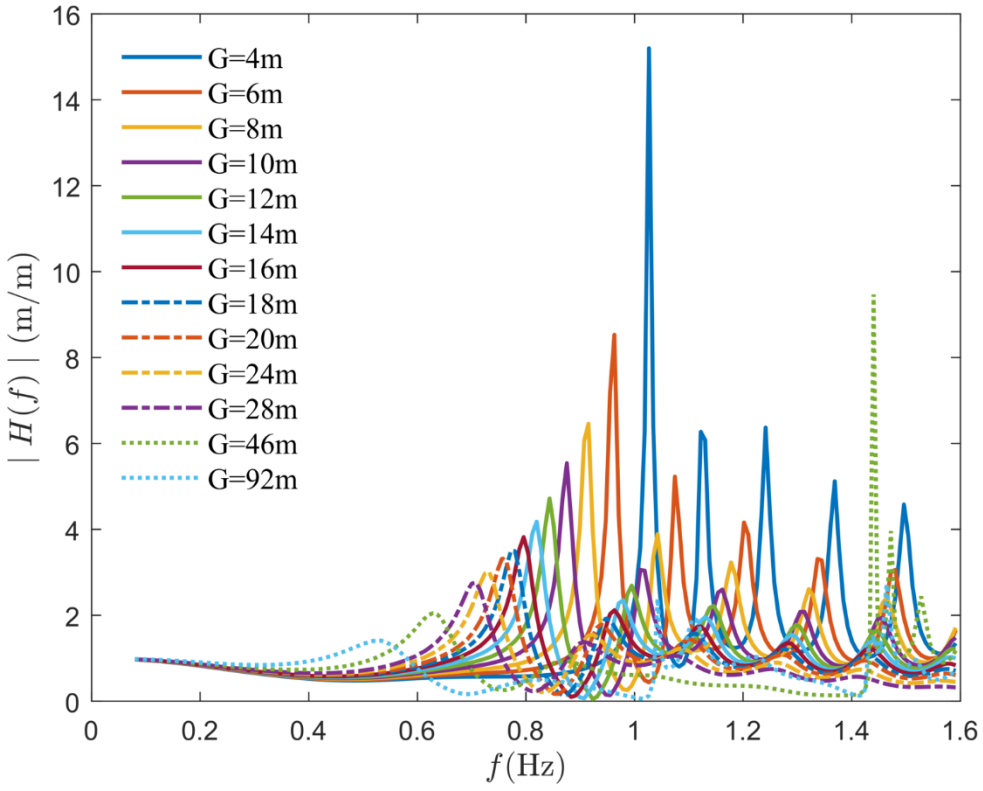

Figure 5.22. Comparison of the surface elevation in the middle of the gap using different gap widths for two fixed barges in a side-by-side configuration. The wave direction is set to 90 degrees and no artificial damping has been applied.

As the gap width reaches above 40 m, some additional peaks appear around $1.4 - 1.6$ Hz. These peaks are the result of the modes crossing the gap. As the gap width increases, it gets easier for the

wave energy to 'escape' from the gap; and thus, the amplitudes of the gap resonances become weaker. For the narrow gaps there are no variation across the gap, meaning that crossing waves are absent and the surface elevation is flat ($n = 0$). However, as the gap width increases, crossing waves are present in the gap and can be used to clarify the additional peaks around $1.4 - 1.6$ Hz. There is little energy dissipation for the crossing gap modes, leading to a greater magnitude. Similar observations have earlier been reported for the surface motions across the gap (Sun et al., 2010; Sun et al., 2015).

Referring to Figure 5.23, interesting observations are unveiled as the gap width reaches one ship-width (46 m). Results with and without artificial damping seems to be identical for gaps above 46 m. Having this in mind, we may conclude that artificial damping is only needed for gap widths lower than one ship width. Seeing this from an engineering perspective, the limit should be at 20-23 m.

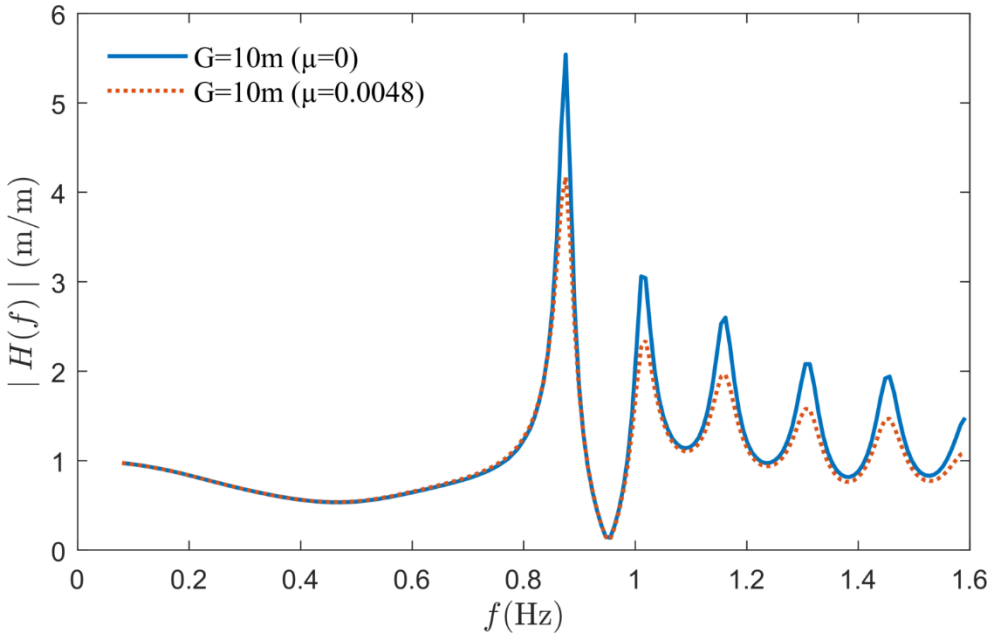

(a)

Figure 5.23. Comparison of the surface elevation in the middle of the gap between two fixed barges in a side-by-side configuration for (a) G=10m, (b) G=16m, (c) G=20m, (d) G=28m, (e) G=35m, (f) G=40m, (g) G=46m, (h) G=50m and (i) G=92m. The blue solid curve refers to the surface elevation without any additional damping. The red dotted line refers to the surface elevation where additional damping of μ=0.0048 have been applied.

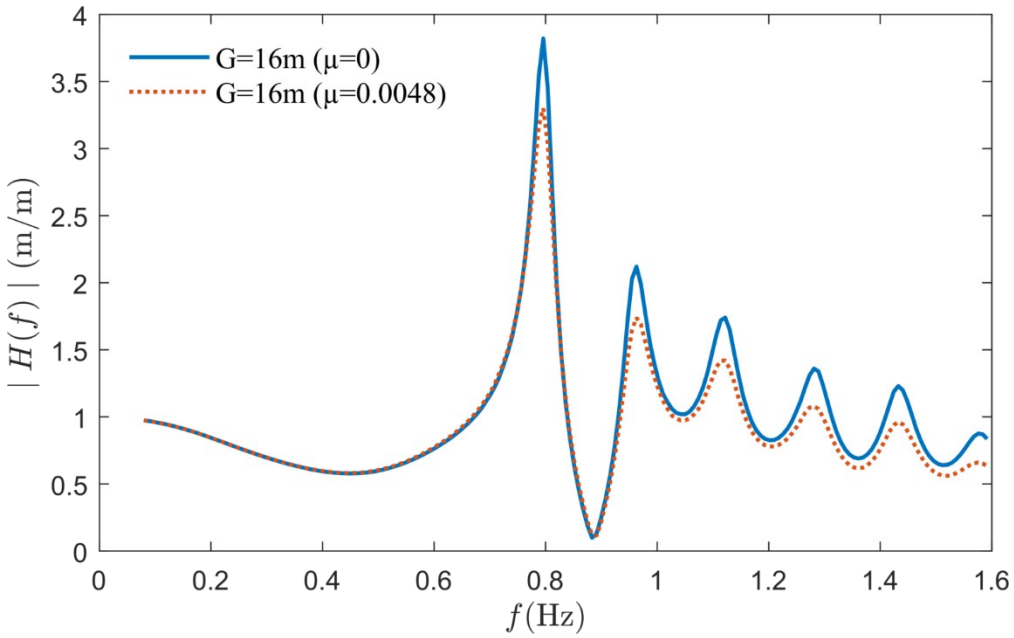

(b)

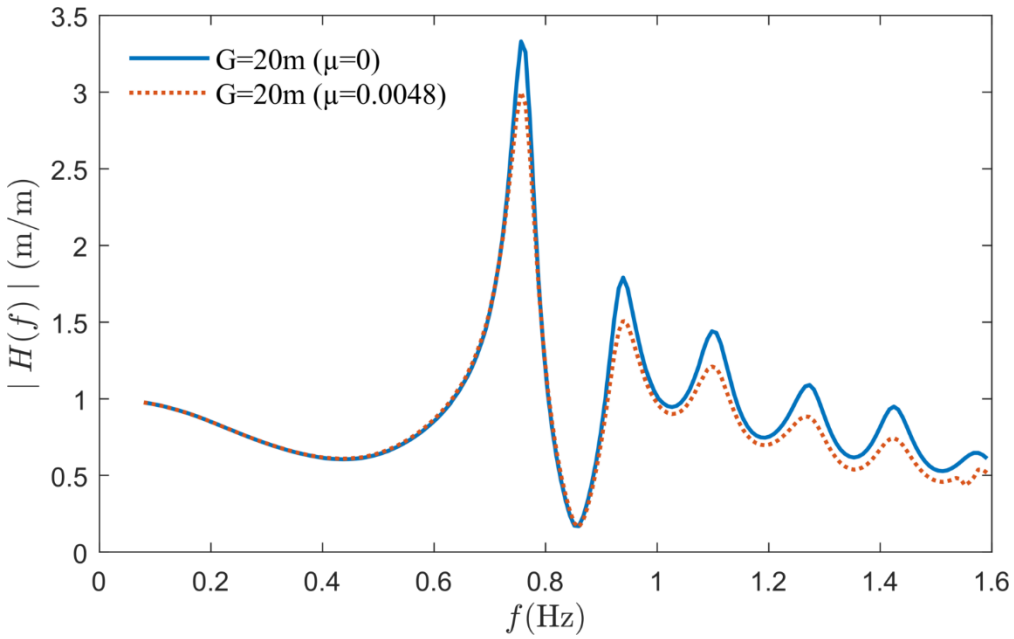

(c)

Figure 5.23. Continued.

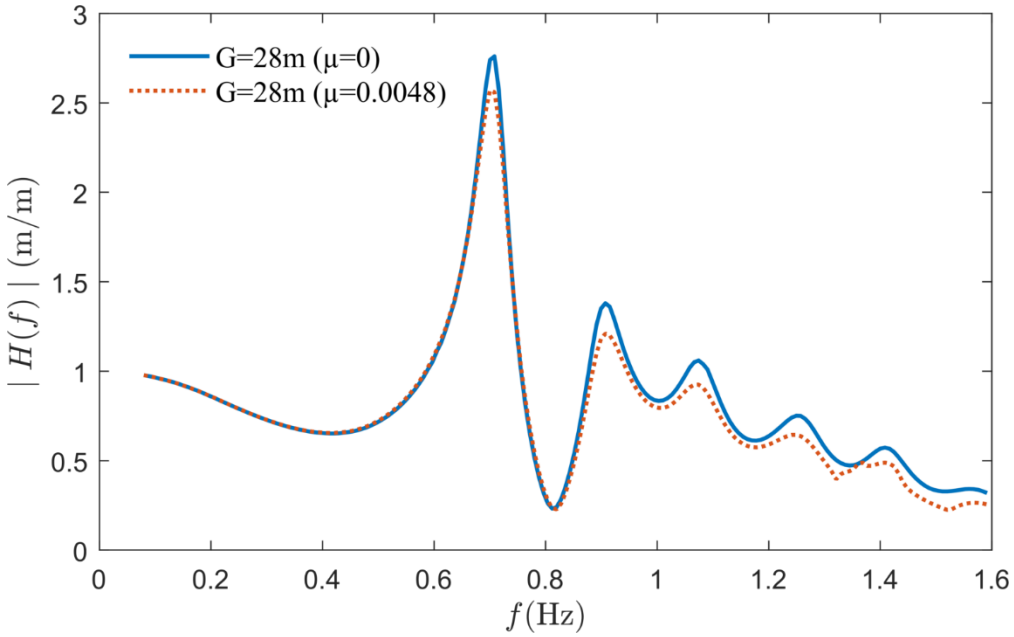

(d)

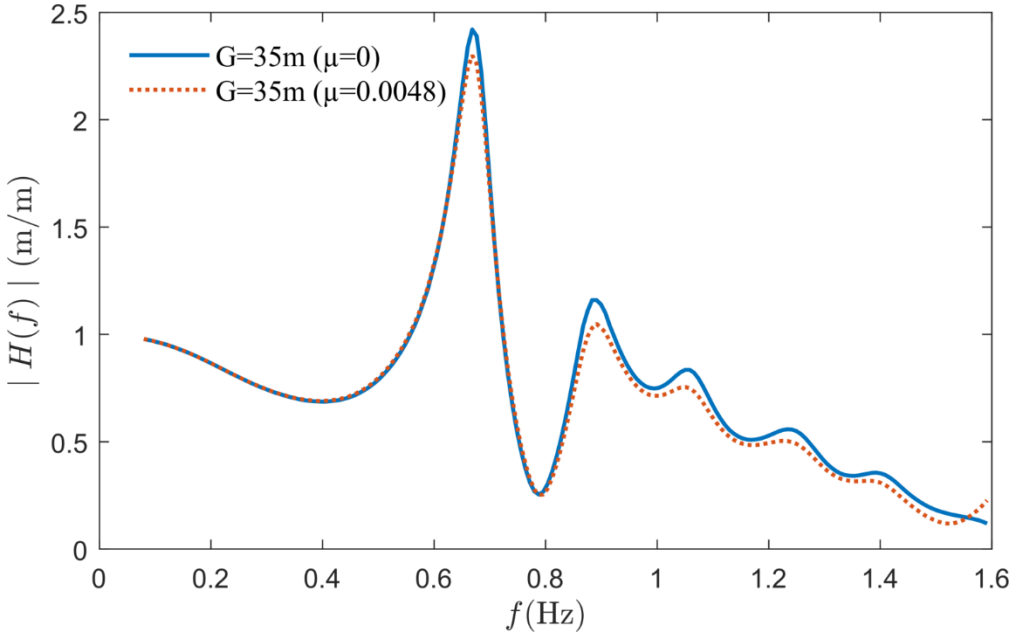

(e)

Figure 5.23. Continued.

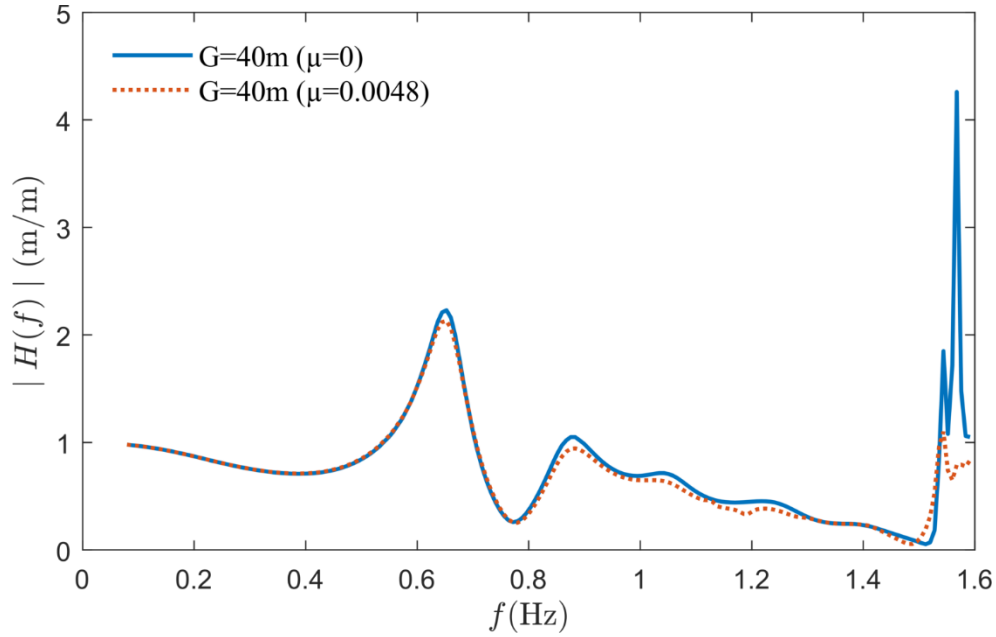

(f)

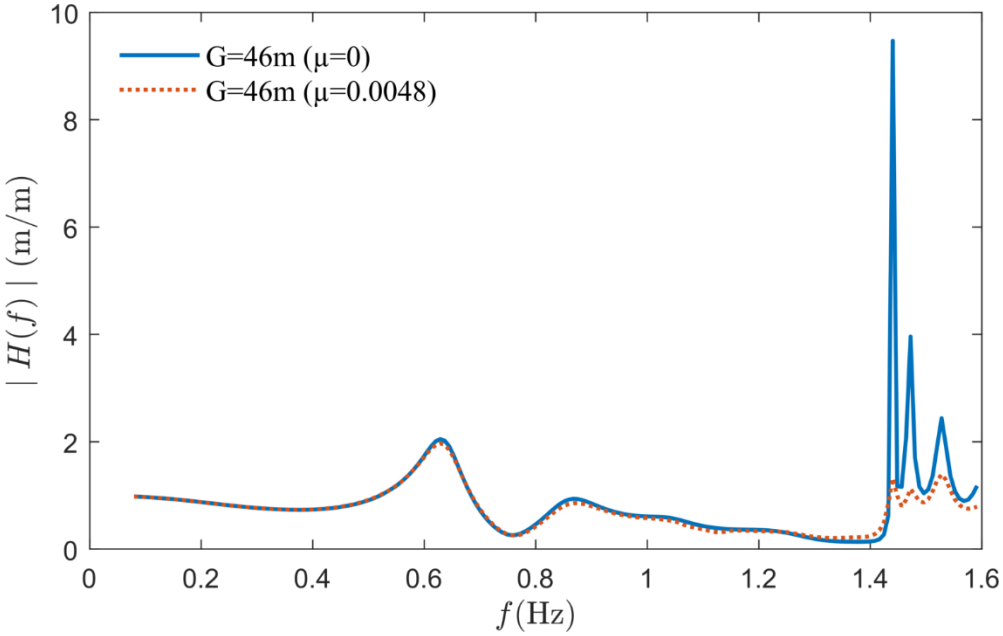

(g)

Figure 5.23. Continued.

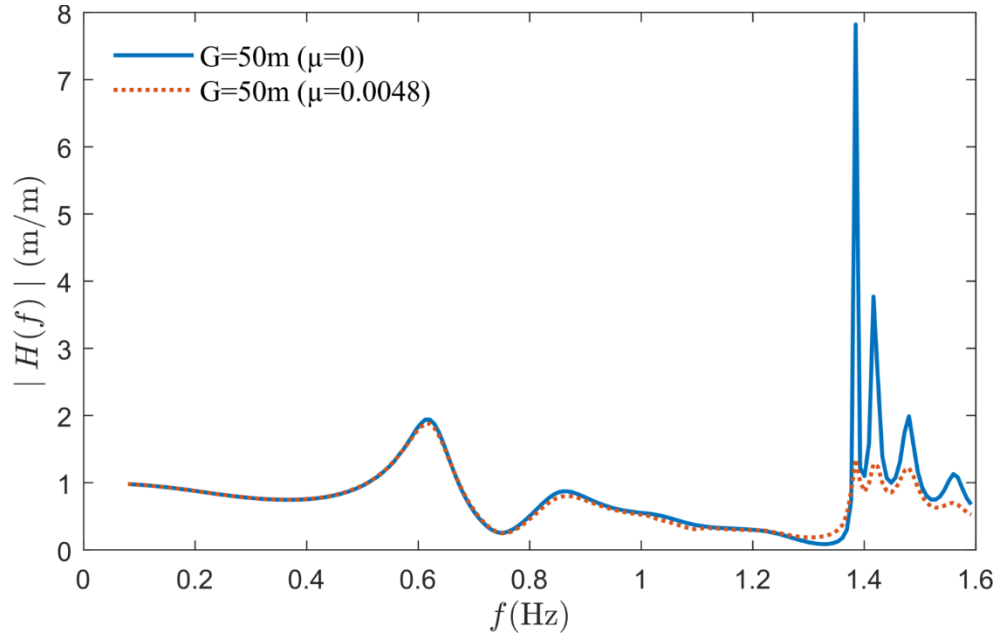

(h)

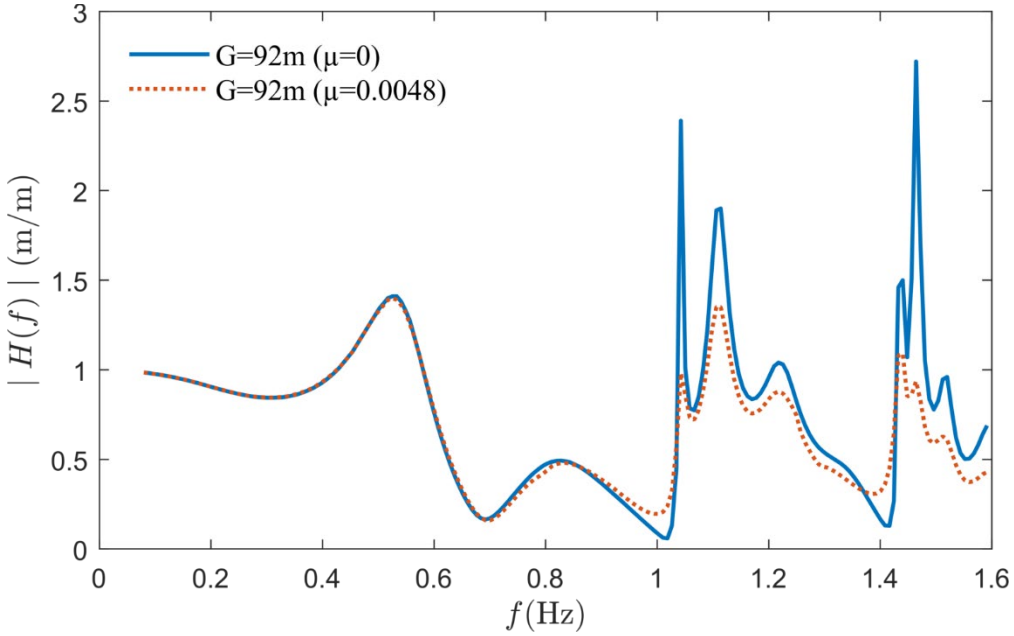

(i)

Figure 5.23. Continued.

5.3.2 A floating and a fixed barge

Figure 5.24 shows the surface elevation in the middle of the gap using 12 different gap widths for one floating and one fixed barge in a side-by-side configuration. Similar observations can be seen from Figure 5.24 as in Figure 5.22. However, as the motion of one barge now has been released, the lowest amplitude of the $m = 1$ mode is seen around 16 m gap width.

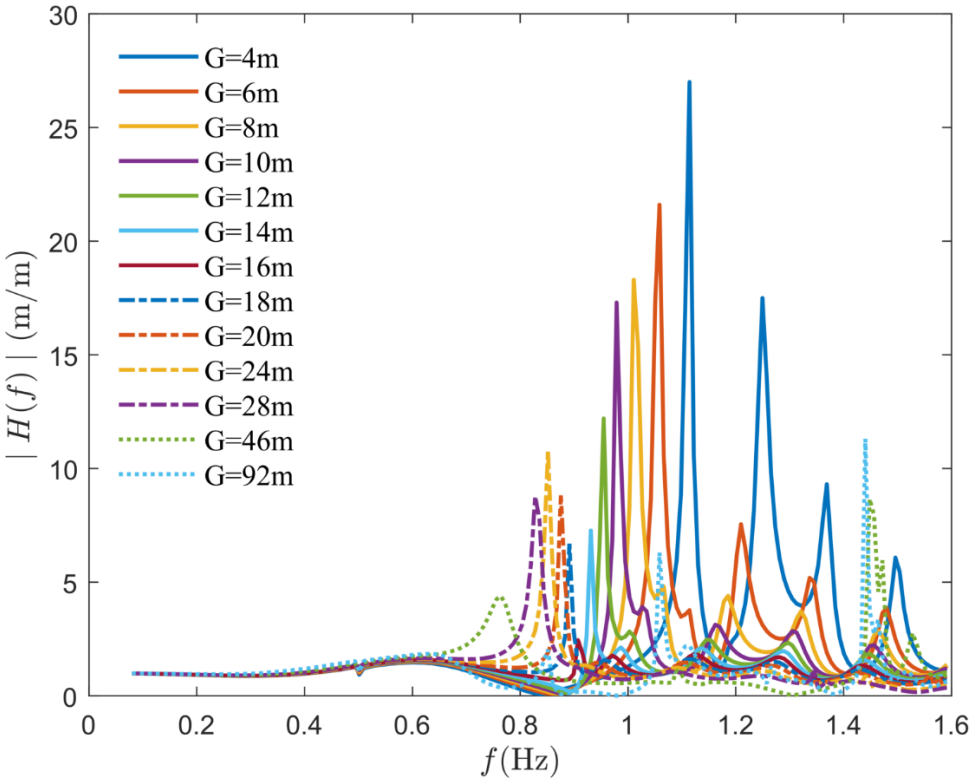

Figure 5.24. Comparison of the surface elevation in the middle of the gap using different gap widths for one floating and one fixed barge in a side-by-side configuration. The wave direction is set to 90 degrees and no artificial damping has been applied.

The amplitude of the gap resonances becomes weaker with increasing gap width until G = 16 m; however, there is a significant increase in magnitude between G = 16 m and G = 24 m. The reason for the canceled gap modes around G =16 m will be investigated further in Section 5.3.3. For the largest gap widths, G = 46 m, and G = 92m, the crossing waves are present in the gap and can be used to clarify the peaks around $1.4 - 1.6$ Hz. Seen in Figure 5.25, results with and without artificial damping seems to be quite satisfactory for gaps above 35 m.

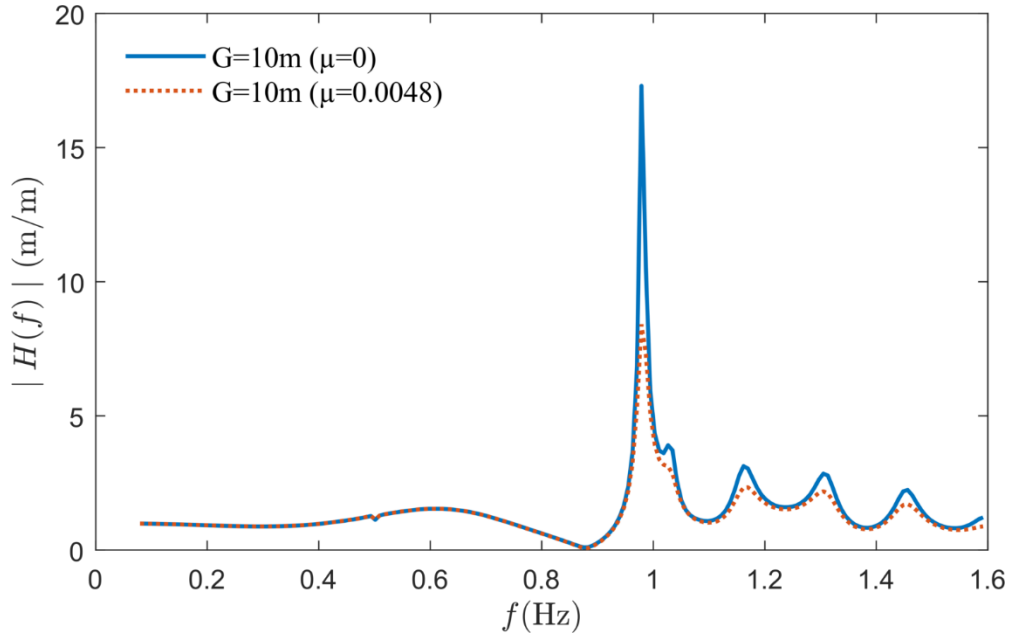

(a)

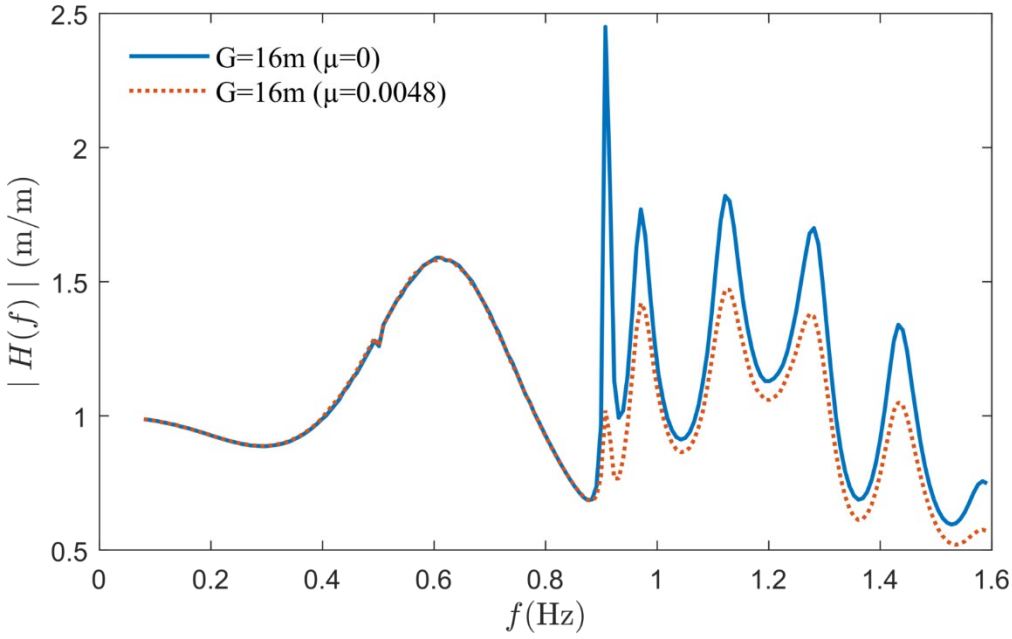

(b)

Figure 5.25. Comparison of the surface elevation in the middle of the gap between one floating and one fixed barge in a side-by-side configuration for (a) G=10m, (b) G=16m, (c) G=20m, (d) G=28m, (e) G=35m, (f) G=40m, (g) G=46m, (h) G=50m and (i) G=92m. The blue solid curve refers to the surface elevation without any additional damping. The red dotted line refers to the surface elevation where additional damping of μ=0.0048 have been applied.

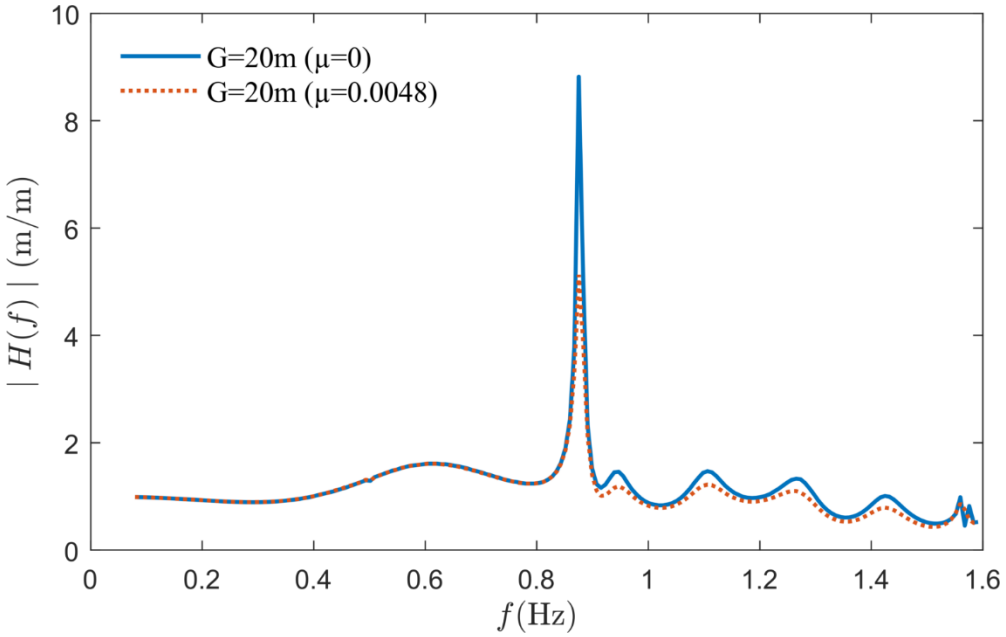

(c)

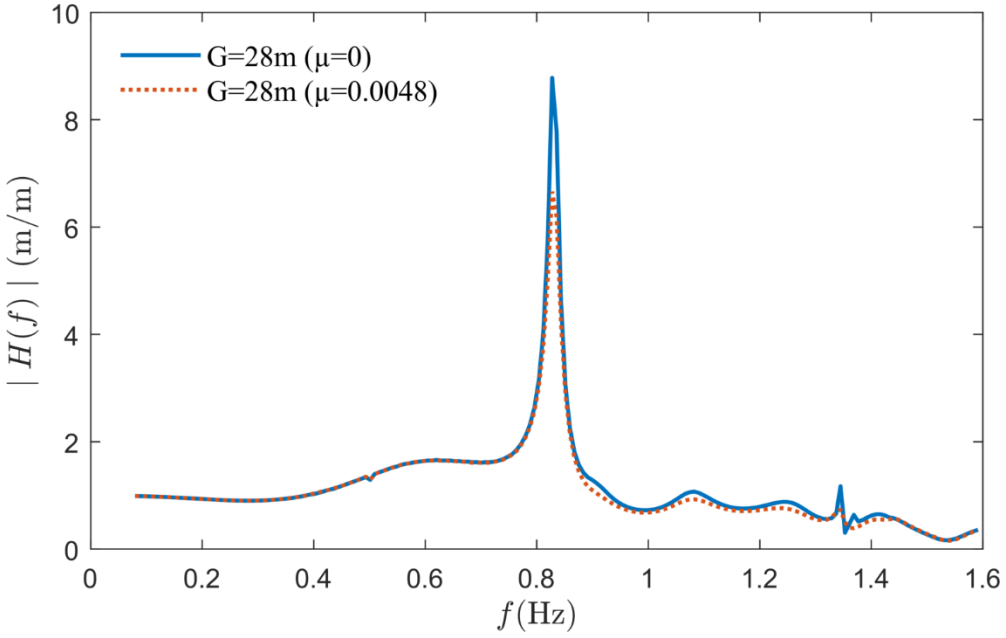

(d)

Figure 5.25. Continued.

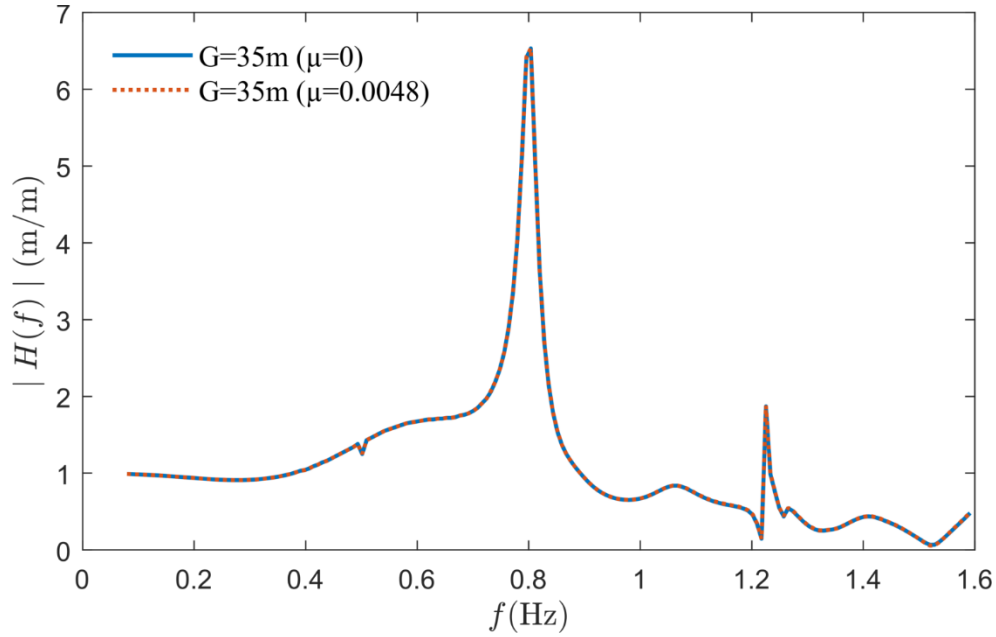

(e)

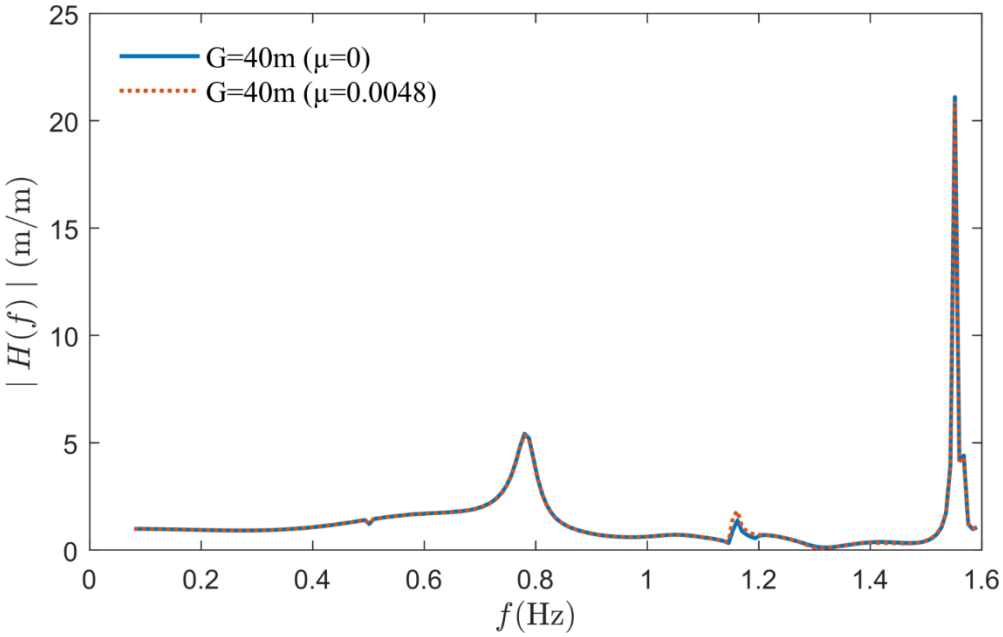

(f)

Figure 5.25. Continued.

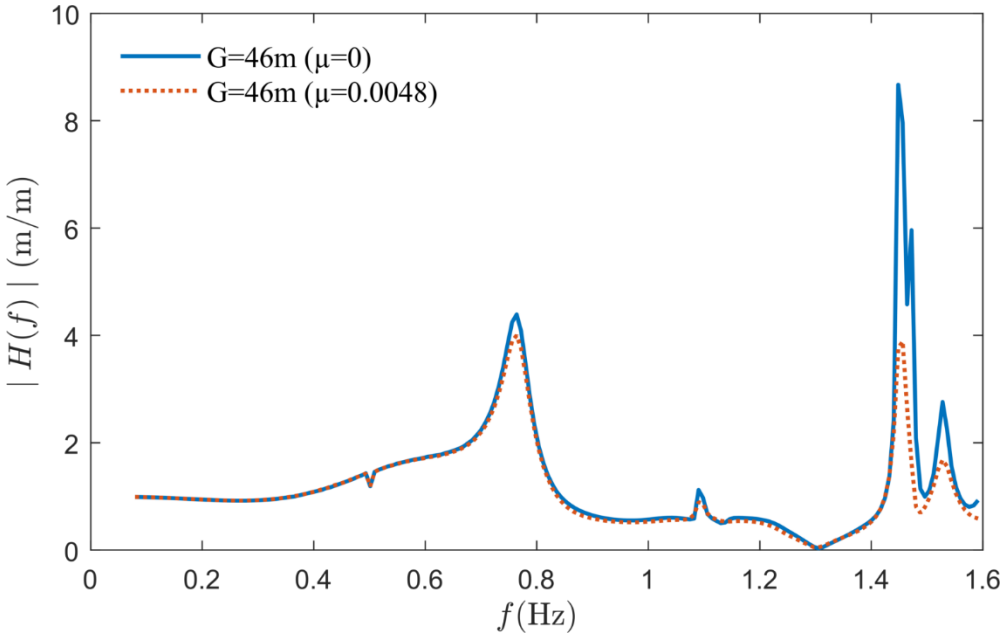

(g)

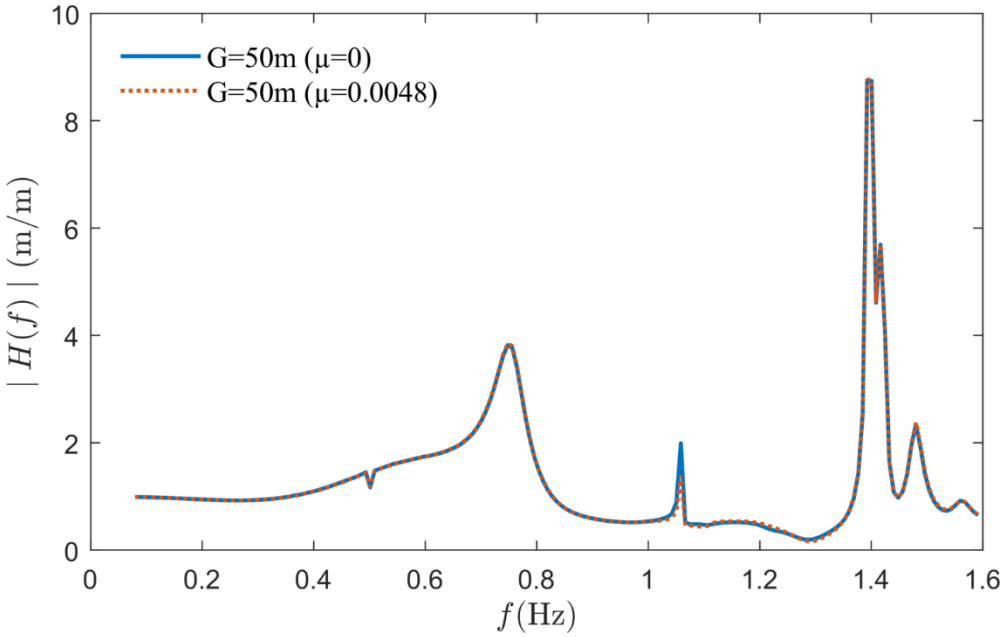

(h)

Figure 5.25. Continued.

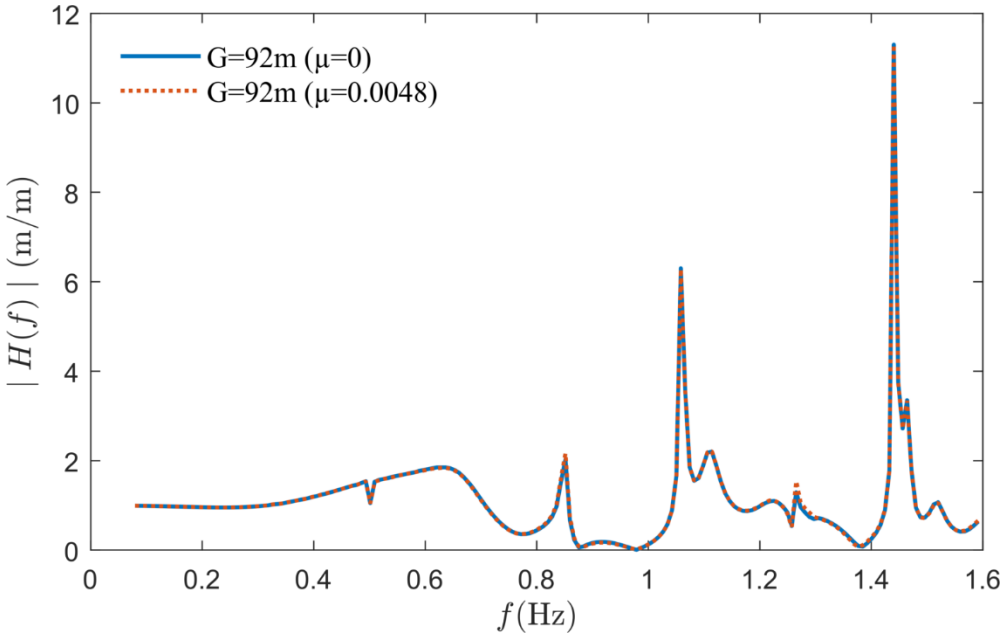

(i)

Figure 5.25. Continued.

5.3.3 The effect at 16 m gap width

It is observed in Figure 5.24 and Figure 5.25 (b) from Section 5.3.2 that the gap RAO at G = 16 m is much smaller compared to those nearby. To explore the reason for this phenomenon, we look at the added mass, as shown in Figure 5.26. One can see the heave and sway have a significant change around $f = 0.8$ Hz. The heave and sway motions are further investigated in Figure 5.27 where they are plotted against the free surface elevations in the gap. Similar effects as in Figure 5.26 are observed around $f = 0.9$ Hz confirming that the coupling between these motions and the $m = 1$ mode contributed to cancel the gap resonant modes.

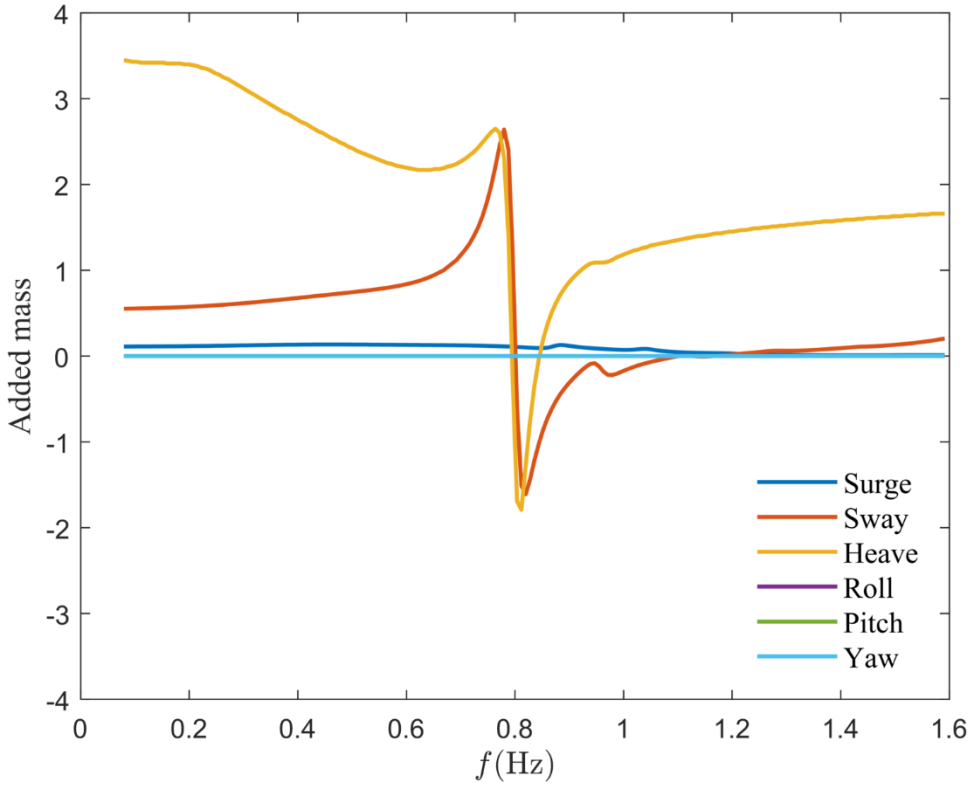

Figure 5.26. Added mass coefficients in 6 DOF for a floating barge in a side-by-side configuration with a fixed barge. The gap width G = 16 m and the wave direction is 90 degrees.

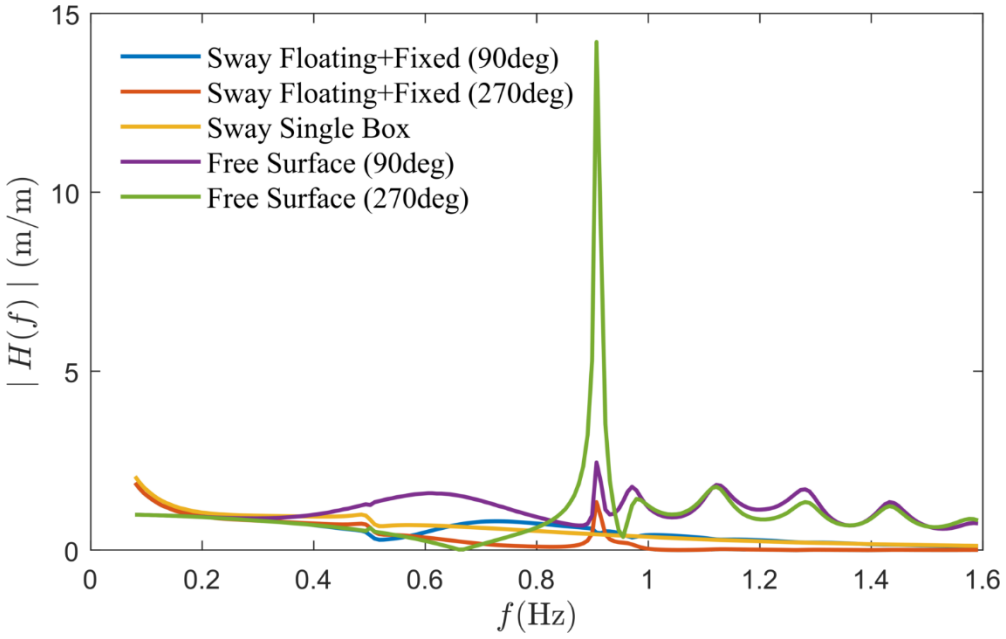

(a)

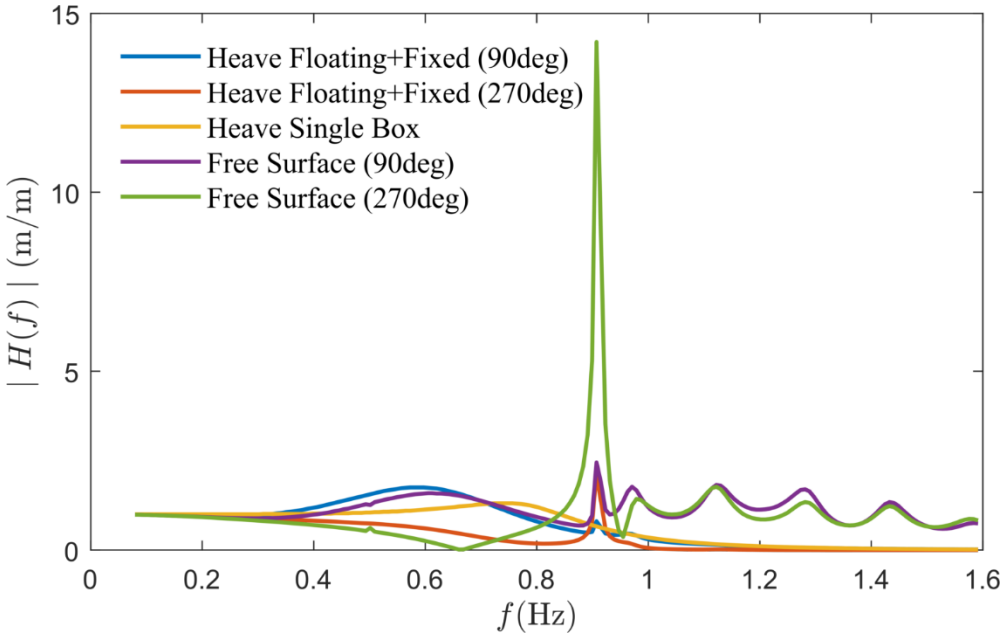

(b)

Figure 5.27. The red and blue curve represents the RAOs in (a) Sway and (b) Heave for a floating box in side by side configuration with 90 and 270 degrees wave directions. The yellow curve represents the RAOs in (a) Sway and (b) Heave for a single floating box with 90 degrees wave direction. The purple and green line represents the surface elevations in the middle of the 16m gap.

Chapter 6

Conclusions and Further work

The resonant responses of the fluid in gaps between two barges are investigated numerically for three different configurations, i.e. (1) both barges fixed, (2) one floating barge plus one fixed barge, and (3) two barges floating. A numerical model is developed based on the commercial software DNV-GL Sesam, whose solver is based on linear potential flow theory. Based on a three-dimensional panel method, this model can be used to evaluate the velocity potentials and hydrodynamic coefficients. The numerical model is first validated against the published results in Zhao et al. (2018*a*) and then used to investigate different cases of the gap resonance. It has been checked such that the meshing in this study is converged. All analyses are undertaken with fine meshes of panel elements, capturing the intense fluid motions within the gap between the two barges. The present numerical results suggest that the coupling between the gap resonance, roll and pitch motions are weak, from the linear analysis. This is because the roll and pitch natural periods are away from those of the gap modes. In contrast, when both barges are fixed, the first gap mode disappears when the barge motions are released – either one barge or both, while the $m = 3$ mode is slightly shifted towards lower frequency. This is observed in both head and beam sea configurations. The results show that the added mass coefficients are changed significantly for heave and sway around $f = 1.03$ Hz, which is the same frequency as that of the first mode for the case where both barges are fixed.

Furthermore, the gap resonances in a series of gap widths are investigated. The results show that the frequencies and magnitude of the peaks of the resonant motions are in general strongly dependent on the spacing, i.e. the gap width. With increasing gap width, it gets easier for the wave energy to 'escape' from the gap, and thus the amplitudes of the gap resonances become weaker. Another interesting phenomenon is that as gap width increases resonant modes (waves) crossing the gap are observed, so the water surface across the gap is not 'flat' anymore. As the boundaries of such waves across the gap are the vessel hulls, where it is more difficult for energy to dissipate – compared to open ends, larger magnitude peaks at high frequencies are observed.

The influence of artificial damping at the free surface is also investigated, mainly focusing on the case with two fixed barges. It is found that the artificial damping does not seem to have significant effect on the gap surface resonant motions as the gap width reaches one ship width. This is not surprising given the fact that wave energy is easier to 'escape' as the gap width increases, so leading to larger energy loss due to waves propagating towards far field.

Some further work on the gap resonance phenomenon is recommended as below:

1) It would be interesting to analyze the surface motions along the gap, so as to learn the variation of the gap resonances.
2) In this study, we have focused on two identical vessels, for the simplicity of the study. However, it would be worthwhile to look at the cases for two side-by-side vessels with different sizes, which is more realistic.
3) CFD simulations or other nonlinear calculations would be helpful to capture the nonlinear coupling which has been totally ignored in this study.

References

Chen, X.B., 2005. Hydrodynamic analysis for offshore LNG terminals. In: Proceedings of the 2nd International Workshop on Applied Offshore Hydrodynamics, Rio de Janeiro.

Dinoi, P., Watai, R.A., Ramos-Castro, H., Gomez-Go ni, J., Ruggeri, F., Souto-Iglesias, A., ~ Simos, A.N., 2014. Analysis of hydrodynamic resonant effects in side-by-side configuration. In: Proceedings of the ASME 2014 33rd International Conference on Offshore Mechanics and Arctic Engineering. June 8–13, San Francisco, California, USA.

DNV-GL, 2017. SESAM User Manual WADAM - Wave Analysis by Diffraction and Morison Theory. Det Norske Veritas.

Eatock Taylor, R., Sun, L., Taylor, P.H., 2008. Gap resonances in focused wave groups. In: 23rd International Workshop on Water Waves and Floating Bodies. April 13–16, Jeju, Korea. http://www.iwwwfb.org/Abstracts/iwwwfb23/iwwwfb23 10.pdf.

Faltinsen O. M., 1990. Sea loads on ships and offshore structures, Cambridge University Press.

Faltinsen, O.M., Rognebakke, O.F., Timokha, A.N., 2007. Two-dimensional resonant piston-like sloshing in a moonpool. J. Fluid Mech. 575, 359–397.

Feng, X., Bai, W., 2015. Wave resonances in a narrow gap between two barges using fully nonlinear numerical simulation. Appl. Ocean Res. 50, 119–129.

Huijsmans, R.H.M., Pinkster, J.A., De Wilde, J.J., 2001. Diffraction and radiation of waves around side-by-side moored vessels. In: 11th International Offshore and Polar Engineering Conference. 17–22 June. International Society of Offshore and Polar Engineers, Stavanger, Norway.

Israeli, M., Orszag, S.A., 1981. Approximation of radiation boundary conditions. J. Comput. Phys. 41, 115–135.

Kim, Y., 2003. Artificial damping in water wave problems I: constant damping. Int. J. Offshore Polar Eng. 13 (2), 88–93.

Kristiansen, T. & Faltinsen, O. M., 2008. Application of a vortex tracking method to the piston-like behaviour in a semi-entrained vertical gap. Appl. Ocean Res. 30 (1), 1–16.

Kristiansen, T. & Faltinsen, O. M., 2012. Gap resonance analyzed by a new domain-decomposition method combining potential and viscous flow DRAFT. Appl. Ocean Res. 34, 198–208.

Lu, L., Teng, B., Sun, L., Chen, B., 2011. Modelling of multi-bodies in close proximity under water waves-Fluid forces on floating bodies. Ocean Eng. 38 (13), 1403–1416.

Molin, B., 2001. On the piston and sloshing modes in moonpools. J. Fluid Mech. 430, 27–50.

Molin, B., Remy, F., Kimmoun, O., Stassen, Y., 2002. Experimental study of the wave propagation and decay in a channel through a rigid ice-sheet. Appl. Ocean Res. 24 (5), 247–260.

Molin, B., Remy, F., Camhi, A., Ledoux, A., 2009. Experimental and numerical study of the gap resonances in-between two rectangular barges. In: 13th Congress of International Maritime Association of Mediterranean.

Pauw, W.H., Huijsmans, R.H.M., Voogt, A., 2007. Advances in the hydrodynamics of sideby-side moored vessels. In: Proceedings of the ASME 2007 26th International Conference on Offshore Mechanics and Arctic Engineering. American Society of Mechanical Engineers, pp. 597–603.

Saitoh, T., Ishida, H., Miao, G.-P., 2000. Influence of gaps between multiple floating bodies on wave forces. China Ocean Engineering 14, 407–422.

Sun, L., Eatock Taylor, R., Taylor, P.H., 2015. Wave driven free surface motion in the gap between a tanker and an FLNG barge. Applied Ocean Research 51, 331-349.

WAMIT, 2013. User Manual Version 7.06, Department of Ocean Engineering, Massachusetts Institute of Technology.

Wang, H., Wolgamot, H. A., Draper, S., Zhao, W., Taylor, P. H., & Cheng L., 2019. Resolving wave and laminar boundary layer scales for gap resonance problems. J. Fluid Mech. 866, 759-775.

Watai, R.A., Dinoi, P., Ruggeri, F., Souto-Iglesias, A., Simos, A.N., 2015. Rankine timedomain method with application to side-by-side gap flow modelling. Appl. Ocean Res. 50, 69–90.

Zhao, W., Yang, J., Hu, Z., Wei, Y., 2011. Recent developments on the hydrodynamics of floating liquid natural gas (FLNG). Ocean Eng. 38 (14), 1555–1567.

Zhao, W., McPhail, F., Efthymiou, M., 2016. Effect of Partially Filled Spherical Cargo Tanks on the Roll Response of a Bargelike Vessel. Journal of Offshore Mechanics and Arctic Engineering 138 (3), 031601.

Zhao, W., Wolgamot, H. A., Taylor, P. H. & Eatock Taylor, R., 2017*a*. Gap resonance and higher harmonics driven by focused transient wave groups. J. Fluid Mech. 812, 905–939.

Zhao, W., McPhail, F. 2017*b*. Roll response of an LNG carrier considering the liquid cargo flow. Ocean Engineering 129, 83-91.

Zhao, W., Pan, Z., Lin, F., Li, B., Taylor, P. H. & Efthymiou, M., 2018*a*. Estimation of gap resonance relevant to side-by-side offloading. Ocean Engineering 153, 1-9.

Zhao, W., Taylor, P.H., Wolgamot, H.A., Eatock Taylor, R., 2018*b*. Linear viscous damping in random wave excited gap resonance at laboratory scale – NewWave analysis and reciprocity. J. Fluid. Struct. 80, 59-76.

Appendix A

Comparison of the time history of the surface elevation with three different values of G.

Figure A.1 below refer to the time histories of the three different gap widths used to validate the present numerical model.

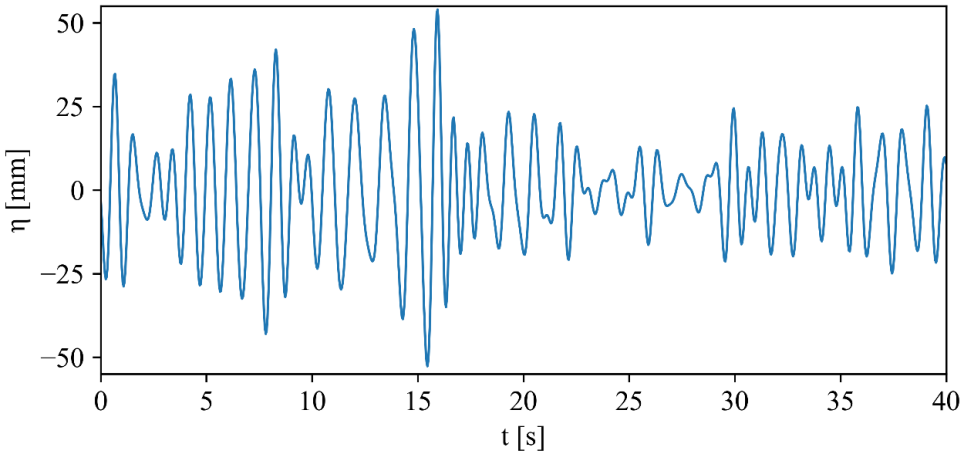

(a)

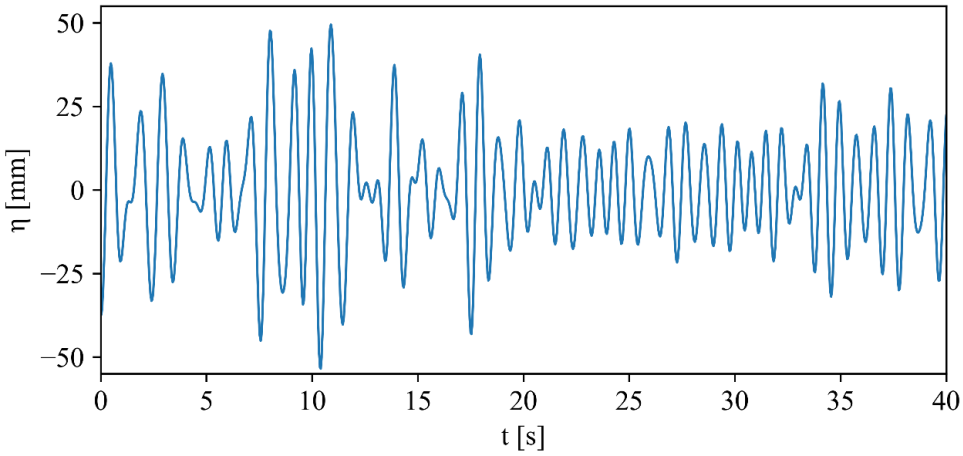

(b)

Figure A.1. Time histories of the surface elevation based on (a) G = 132mm, (b) G = 66 mm, and (c) G = 33 mm. η is the amplitude measured in mm, and t is the time measured in seconds.

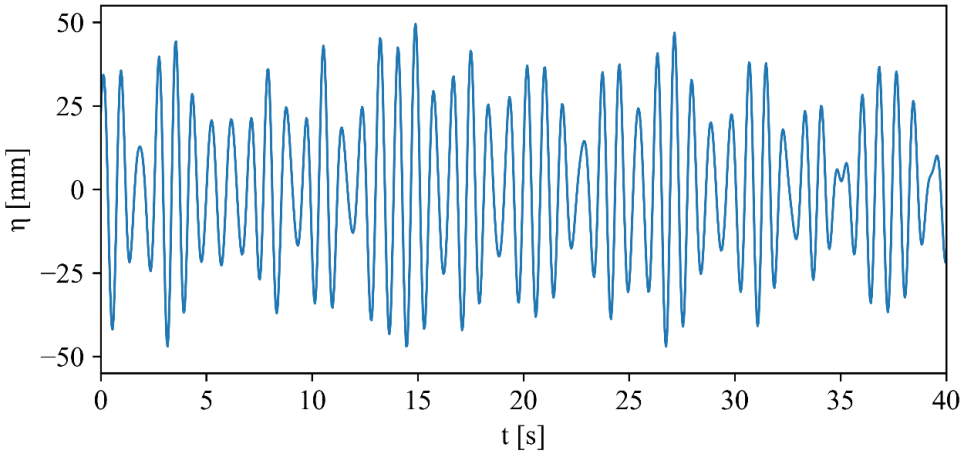

(c)

Figure A.1. Continued.

Appendix B

Greens theorem

Given the functions *f* and *g* defined in Ω, bounded by the boundary *δ*Ω. Greens second identity relate the volume integral to a surface integral,

$$\int_{\Omega} (f\nabla^2 g - g\nabla^2 f)dV = \int_{\delta\Omega} \left(f\frac{\partial g}{\partial n} - g\frac{\partial f}{\partial n}\right) dS$$

We consider two Laplacian potentials, φ and ψ defined in the volume *V*, with boundary *S*. It follows from Greens theorem that.

$$\int_{S} \left(\varphi\frac{\partial \psi}{\partial n} - \psi\frac{\partial \varphi}{\partial n}\right) dS = 0$$

We let ψ be a source with field point x and source point ξ. The two-dimensional source, $\psi = ln\ r$, where $r = |x-\xi| = p\ (x - \xi)\ 2 + (z - \zeta)$. When $r = 0$ then ψ becomes singular and does not satisfy $\nabla 2\psi = 0$. Except at the singular point the function is Laplacian. We enclose the singular point $x - \xi$ by a circle or half circle if *x* is on the fluid boundary. The contributions from the limits of the circle/half circle around the singularity could be found by Taylor-expansion. The resulting expression is,

$$\int_{S} \left(\varphi(\xi)\frac{\partial G(\xi;x)}{\partial n_\xi} - G(\xi;x)\frac{\partial \varphi(\xi)}{\partial n_\xi}\right) d\xi = \begin{cases} 0 \\ \pi\varphi(x) \\ 2\pi\varphi(x) \end{cases}$$

Where 0 refers to outside the fluid domain, $\pi\varphi(x)$ refers to the boundary and $2\pi\varphi(x)$ refers to inside the fluid domain.